Dataset Distillation Fixes Dataset Reconstruction Attacks

Noel Loo*, **Ramin Hasani, Mathias Lechner, Daniela Rus**

Computer Science and Artificial Intelligence Lab (CSAIL)
Massachusetts Institute of Technology (MIT)
Cambridge, 02139, MA
Correspondence to loo@mit.edu

Modern deep learning requires large volumes of data, which could contain sensitive or private information which cannot be leaked. Recent work has shown for homogeneous neural networks a large portion of this training data could be reconstructed with only access to the trained network parameters. While the attack was shown to work empirically, there exists little formal understanding of its effectiveness regime, and ways to defend against it. In this work, we first build a stronger version of the dataset reconstruction attack and show how it can provably recover their *entire training set* in the infinite width regime. We then empirically study the characteristics of this attack on two-layer networks and reveal that its success heavily depends on deviations from the frozen infinite-width Neural Tangent Kernel limit. More importantly, we formally show for the first time that dataset reconstruction attacks are a variation of dataset distillation. This key theoretical result on the unification of dataset reconstruction and distillation not only sheds more light on the characteristics of the attack but enables us to design defense mechanisms against them via distillation algorithms.

1. Introduction

Neural networks have been shown to generalize well to unseen test data on a large range of tasks, despite achieving zero loss on training data (Zhang et al., 2017, 2021). But this performance is useless if neural networks cannot be used in practice due to safety and security issues (Gruenbacher et al., 2022; Grunbacher et al., 2021; Lechner et al., 2020, 2021; Xiao et al., 2021, 2022). A fundamental question in the security of neural networks is how much information is *leaked* via this training procedure, that is, can adversaries with access to trained models, or predictions from a model, infer what data was used to train the model? Ideally, we would want to ensure that our models are resistant to these attacks. However, in practice, we see that this ideal is commonly violated. One heinous violation of this principle is the phenomenon of memorization (Arpit et al., 2017; Carlini et al., 2019; Feldman, 2020; Feldman and Zhang, 2020), where trained networks can be shown to replicate their training data at test time in generative models. A more extreme example of memorization is presented in Haim et al. (2022), where the authors show that it is possible to recover a large subset of the training data given only the trained network parameters.

The existence of this attack begs many follow-up questions, namely: "*Under what circumstances is this attack successful?*"; "*What are properties of these recovered images?*"; and "*What can we do to defend against these attacks?*" In this paper, we consider a stronger variant of the attack presented in Haim et al. (2022), provide novel theoretical and empirical insights about dataset reconstruction attacks, and provide answers to the above questions. In particular, we make the following new **contributions**:

*Code Repository: https://github.com/yolky/distillation_fixes_reconstruction

A Stronger Reconstruction Attack. We design a stronger version of Haim et al. (2022)'s dataset reconstruction attack that can provably reconstruct the *entire* training set for networks in the neural tangent kernel (NTK) (Jacot et al., 2018) regime when trained under mean squared error (MSE) loss. This attack transfers to finite networks with its success dependent on deviations from the NTK regime.

Reconstruction is a Variant of Distillation. We formally prove and empirically show that dataset reconstruction attack is a variant of *dataset distillation*. More specifically, the reconstruction loss is equal to the loss of the kernel-inducing points (KIP) (Nguyen et al., 2021a,b) dataset distillation algorithm, under a different norm, plus a variance-controlled term. Furthermore, we can retrain models using recovered images and achieve high performance.

Defending Against Reconstruction Attacks. Motivated by the fundamental connection between reconstruction and dataset distillation, we design a defense mechanism and show that by training on a distilled dataset, we can retain performance while ensuring that only distilled images are recovered and not the training data.

2. Background and Related Works

Machine Learning Privacy. A large body of work studies how to extract sensitive information from trained models. This is problematic as legislation such as HIPAA and GDPR enforce what data can and cannot be published/used (Centers for Medicare & Medicaid Services, 1996; European Commission, 2016). Quantifying the influence of training examples leads to the topic of influence functions (Koh and Liang, 2017), and Membership-inference attacks (Shokri et al., 2016), which try to infer whether particular examples were used in training. Defending against these attacks is the study of *differential privacy*, which quantifies and limits the sensitivity of models to small changes in training data (Abadi et al., 2016; Dwork et al., 2006). Likewise, the field of *machine unlearning* tries to remove the influence of training examples post-training (Bourtoule et al., 2019). Without these defense techniques, trained networks have been shown to leak information (Rigaki and Garcia, 2020). For generative language models, (Carlini et al., 2019) show large language models often reproduce examples in the training corpus verbatim. *Model inversion* techniques aim to recreate training examples by looking at model activations (Fredrikson et al., 2015; He et al., 2019; Yang et al., 2019). This memorization phenomenon can be shown to be necessary to achieve high performance under certain circumstances (Brown et al., 2021; Feldman and Zhang, 2020).

Dataset Reconstruction. Recent work (Haim et al., 2022) has shown that it is possible to reconstruct a large subset of the training data from trained networks by exploiting the implicit biases of neural networks. Specifically, they note that homogeneous neural networks trained under a logistic loss converge in direction to the solution of the following max-margin problem (Ji and Telgarsky, 2020; Lyu and Li, 2020):

$$\underset{\theta'}{\operatorname{argmin}} \frac{1}{2}\|\theta'\|_2^2 \quad s.t. \quad \forall i \in [n], \quad y_i f_{\theta'}(x_i) \geq 1, \tag{1}$$

Where $\{x_i, y_i\}$ is the training set with images x_i and labels $y_i \in \{+1, -1\}$, and $f_{\theta'}(x)$ the neural network output with parameters θ'. (Haim et al., 2022) shows that by taking a trained neural network and optimizing images (and dual parameters) to match the Karush–Kuhn–Tucker (KKT) conditions of the max-margin problem, it is possible to reconstruct training data. This is an attack that causes leakage of training data. Here, we consider a stronger variant of the attack that requires training under mean-squared error (MSE) loss.

Neural Tangent Kernel. One method of understanding the generalization of neural networks is through the lens of the neural tangent kernel (NTK) (Arora et al., 2019; Jacot et al., 2018). Specifically, this theory states that networks behave like first-order Taylor expansions of network parameters about their initialization as network

width approaches infinity (Lee et al., 2019). Furthermore, the resulting feature map and kernel converge to the NTK, and this kernel is frozen throughout training (Arora et al., 2019; Jacot et al., 2018). As a result, wide neural networks are analogous to kernel machines, and when trained with MSE loss using a support set X_S with labels y_S result in test predictions given by

$$\hat{y}_T = K_{TS}K_{SS}^{-1}y_S$$

With K being the NTK. For fully-connected networks, this kernel can be computed exactly very quickly (as they reduce to arc-cosine kernels), but for larger convolutional networks, exact computation slows down dramatically (Arora et al., 2019; Zandieh et al., 2021). In practice, it has been shown that networks often deviate far from the frozen-kernel theoretical regime, with the resulting empirical NTKs varying significantly within the first few epochs of training before freezing for the rest (Aitken and Gur-Ari, 2020; Fort et al., 2020; Hanin and Nica, 2020; Loo et al., 2022b; Tsilivis and Kempe, 2022). In this paper, we use the NTK theory to gain a better understanding of these reconstruction attacks.

Dataset Distillation. Dataset distillation aims to construct smaller synthetic datasets which accurately represent larger datasets. Specifically, training on substantially smaller *distilled dataset* achieves performance comparable to the full dataset, and far above random sampling of the dataset (Loo et al., 2022a; Nguyen et al., 2021a,b; Wang et al., 2018; Zhao and Bilen, 2021; Zhao et al., 2021; Zhou et al., 2022). There are many algorithms for this, ranging from methods that directly unroll computation (Wang et al., 2018), try to efficiently approximate the inner unrolled computation associated with training on distilled data (Loo et al., 2022a; Nguyen et al., 2021b; Zhou et al., 2022), and other heuristics (Zhao and Bilen, 2021; Zhao et al., 2021). One algorithm is kernel-induced points (KIP) (Nguyen et al., 2021a,b), which leverages NTK theory to derive the following loss:

$$\mathcal{L}_{KIP} = \frac{1}{2}\|y_t - K_{TS}K_{SS}^{-1}y_S\|_2^2.$$

The loss indicates the prediction error of infinite width networks on distilled images X_S and labels y_S, which are then optimized. We bring up dataset distillation as we show in this paper that our dataset reconstruction attack is a generalization of KIP, and that dataset distillation can be used to defend against the attack.

3. A Stronger Reconstruction Attack

Haim et al. (2022) considers the scenario where the attacker only has access to the final trained network parameters. Their attack requires that the networks are homogeneous and are trained for many epochs until convergence so that the network converges in direction to the final KKT point of Eq. 1. Here, we consider the case where the attacker also has access to the network's initialization. We further assume that the model was trained under MSE loss. While having access to the initialization is a strong assumption, we make this change for the following reasons. Firstly, we find that the attack presented in Haim et al. (2022) is incredibly brittle. Namely, we were unable to reliably reproduce their results without careful hyperparameter tuning, and careful network initialization strategies. Furthermore, outside of the top few reconstructions, the overwhelming majority of reconstructions ($> 70\%$) are of poor quality (more in-depth discussions in Section S1). Our attack does not suffer from these problems and is consistently reproducible.

We first present our attack and later discuss its advantages. Consider a neural network trained under MSE loss, $\mathcal{L} = \frac{1}{2}\sum_{i=0}^{N-1}(y_i - f_\theta(x_i))^2$, for $x_i, y_i \in X_T, y_T$, being the training set datapoints and labels. Now further assume that the network is trained under gradient flow and that the network is approximately in the lazy/NTK regime, that is, it behaves like a first-order Taylor expansion of the network outputs (Chizat et al., 2019):

$$f_\theta(x) \approx f_{lin,\theta}(x) = f_{\theta_0}(x) + (\theta - \theta_0)^\intercal \nabla_\theta f_{\theta_0}(x) \tag{2}$$

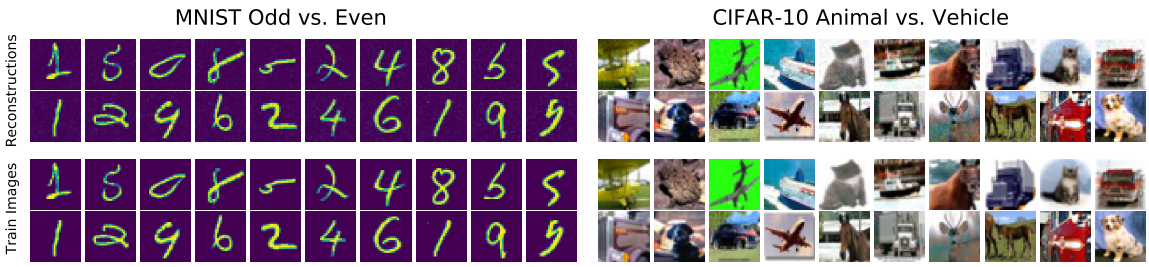

Fig. 1: Reconstructed images (top) vs closest training images (bottom) for MNIST Odd vs. Even, and CIFAR-10 Animal vs. Vehicle Classification. Reconstructions were made from 4096-width two hidden layer fully-conneted networks trained with standard dynamics and low learning rates. Apart from small amonts of noise, the original images and their reconstructions are visually indistinguishable.

Lee et al. (2019) shows that the time evolution of the network parameters in this regime is given by:

$$\theta(t) = \theta_0 - \nabla_\theta f_{\theta_0}(X_T)^\intercal K_0^{-1} \left(I - e^{-\eta K_0 t}\right) \left(f_{\theta_0}(X_T) - y_T\right)$$

With η the learning rate and K_0 the finite-width/empirical NTK evaluated at θ_0. Namely, the final change in parameters is given by:

$$\Delta\theta = \theta_f - \theta_0 = \nabla_\theta f_{\theta_0}(X_T)^\intercal K_0^{-1}(y_T - f_{\theta_0}(X_T)) \tag{3}$$

Notably, this is the solution to the following optimization problem:

$$\begin{aligned} &\underset{\Delta\theta}{\operatorname{argmin}} \frac{1}{2}\|\Delta\theta\|_2^2 \quad s.t. \\ &\Delta\theta^\intercal \nabla_\theta f_{\theta_0}(X_T) = y_T - f_{\theta_0}(X_T) \end{aligned} \tag{4}$$

The corresponding KKT conditions are:

$$\Delta\theta = \alpha^\intercal \nabla_\theta f_{\theta_0}(X_T) \tag{5}$$

$$\Delta\theta^\intercal \nabla_\theta f_{\theta_0}(X_T) = y_T - f_{\theta_0}(X_T) \tag{6}$$

With α being the set of dual parameters. Equation (5) ensures we are at a stationary point, while Equation (6) ensures that the labels are correct. Like with (Haim et al., 2022), we can directly optimize the reconstruction images and dual parameters (X and α, respectively) to match these KKT conditions, given a network's final parameters and initialization to get $\Delta\theta$. In practice, we only need to optimize Equation (5), for reasons we will describe next, leading to our reconstruction loss:

$$\mathcal{L}_{\text{Reconstruction}} = \|\Delta\theta - \alpha^\intercal \nabla_\theta f_{\theta_0}(X_T)\|_2^2 \tag{7}$$

Reconstruction in Infinite Width. Next, we show that this formulation of the attack recovers the *entire* training set for infinite-width models. We further assume that the training data lies on the unit hypersphere.

Theorem 1. *If $\mathcal{L}_{reconstruction} = 0$ (from Eq. 7), then we reconstruct the entire training set in the infinite-width limit, assuming that training data lies on the unit hypersphere.*

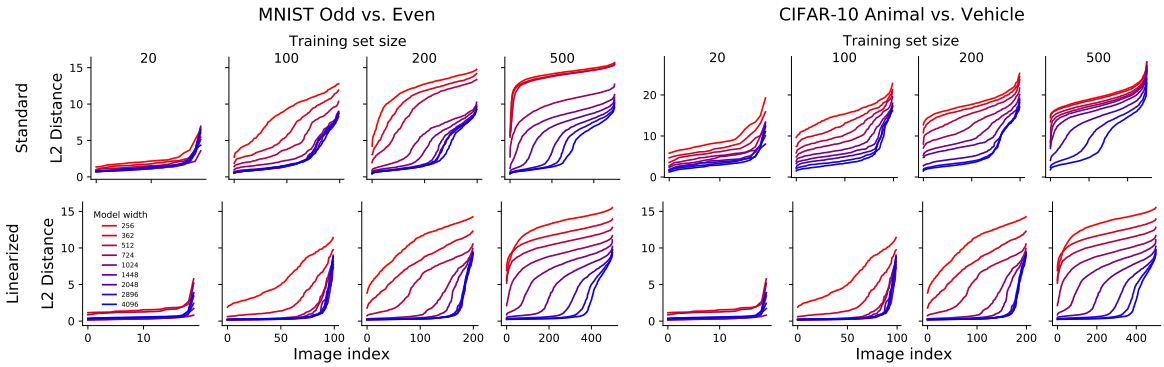

Fig. 2: Reconstruction quality curves for the MNIST Odd vs. Even and for CIFAR-10 Animal vs. Vehicle classification. We either used standard dynamics (top) or linearized dynamics (bottom) and varied both the size of the training set and model width. Smaller datasets are easier to reconstruct while wider models can reconstruct more images, with linearization helping in both scenarios.

Proof. Define $k_\theta(x,x') = \nabla_\theta f_\theta(x)^\intercal \nabla_\theta f_\theta(x')$, that is, the finite-width/empirical NTK function. We know as network width $w \to \infty$, $\Delta\theta = \sum_{\alpha_i, x_i \in \alpha^T, X_T} \alpha_i \nabla_{\theta_0} f_{\theta_0}(x_i)$, with $\alpha^T = K_{\theta_0,TT}^{-1} y_T$, with X_T being the training set, y_T the training labels, and $K_{\theta_0,TT}$ the finite-width NTK evaluated on the training set. Our attack then becomes:

$$\begin{aligned}
&\left\| \Delta\theta - \sum_{\alpha_j x_j \in \alpha^R, X_R} \alpha_j \nabla_{\theta_f} f_{\theta_f}(x_j) \right\|_2^2 \\
&= \left\| \sum_{\alpha_i, x_i \in \alpha^T, X_T} \alpha_i \nabla_{\theta_0} f(x_i) - \sum_{\alpha_j x_j \in \alpha^R, X_R} \alpha_j \nabla_{\theta_f} f_{\theta_f}(x_j) \right\|_2^2 \\
&= \left\| \sum_{\alpha_i, x_i \in \alpha^T, X_T} \alpha_i k_{\theta_0}(x_i, \cdot) - \sum_{\alpha_j x_j \in \alpha^R, X_R} \alpha_j k_{\theta_f}(x_j, \cdot) \right\|_2^2
\end{aligned}$$

With T and R referring to the training and reconstruction set, respectively. As $w \to \infty$ we know that $k_{\theta_0}, k_{\theta_f} \to k_{NTK}$. Furthermore, define

$$\begin{aligned}
P_T &= \sum_{\alpha_i, x_i \in \alpha^T, X_T} \alpha_i \delta(x_i) \\
P_R &= \sum_{\alpha_j, x_j \in \alpha^R, X_R} \alpha_j \delta(x_j)
\end{aligned}$$

as measures associated with our trained network and reconstruction, respectively, and $\mu_* = \int_\Omega k_{NTK}(x, \cdot) dP_*(x)$, with $\Omega = S^d$, with d being the data dimension (we assume that the data lies on the unit hypersphere). μ_T and μ_R are now kernel embeddings of our trained network and reconstruction, respectively. Our reconstruction loss becomes: $\|\mu_T - \mu_R\|^2_{\mathcal{H}_{NTK}}$. This is the familiar maximum-mean discrepancy (MMD) (Gretton et al., 2012). Furthermore, we note that P_T, P_R are signed Borel measures (since α are finite and our reconstruction/training sets are on the unit sphere). The NTK is universal over the unit sphere (Jacot et al., 2018), implying that the map $\mu : \{\text{Family of signed Borel measures}\} \to \mathcal{H}$ is injective Sriperumbudur et al. (2011), meaning that we are able to **recover the entire training set**, provided that $\alpha_i \neq 0$, which happens almost surely (see Section S2). □

Note that in practice we do not enforce the unit sphere requirement on the data, and we still see high reconstruction quality, which we show in Section 4. This mapping from the network tangent space to image space also sheds light on the success of gradient leakage attacks (Zhu et al., 2019), in which gradients are used to find training batch examples.

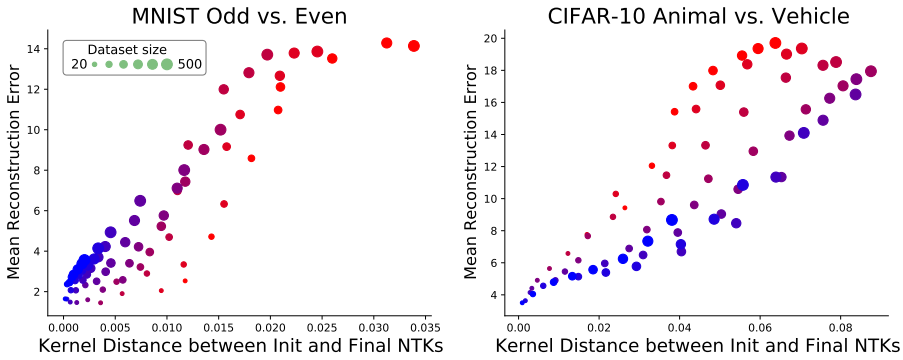

Fig. 3: Mean reconstruction error vs. the kernel distance from the initialization kernel to the final kernel. The mean reconstruction error, measured as the average value of the reconstruction curve, is strongly correlated with how much the finite-width NTK evolves over training. Dataset size is given by dot size, while the color indicates model width (see Figure **2**).

4. Dataset Reconstruction for Finite Networks

While the attack outlined in Theorem 1 carries fundamental theoretical insights in the infinite-width limit, it has limited practicality as it requires access to the training images themselves to compute the kernel inner products. How does the attack work for finite-width neural networks, and under what circumstances is this attack successful?

To answer these questions, we follow the experimental protocol of Haim et al. (2022), where we try to recover images from the MNIST and CIFAR-10 datasets on the task of odd/even digit or animal/vehicle classification for MNIST and CIFAR-10, respectively. We vary the size of the training set from 10 images per class to 250 images per class (500 total training set size). We consider two hidden layer neural networks with biases using standard initialization (as opposed to NTK parameterization or the initialization scheme proposed in Haim et al. (2022)). We vary the width of the neural networks between 256 and 4096 to see how deviations from the infinite-width regime affect the reconstruction quality. Furthermore, it is known that for finite-width networks the finite-width NTK varies over the course of training, deviating from the infinite-width regime. We can force the kernel to be frozen by considering *linearized* training, where we train a first-order Taylor expansion of the network parameters around its initialization (see Equation (2)). We consider both networks under standard (unmodified) dynamics and linearized dynamics.

We train these networks for 10^6 iteration using full-batch gradient descent with a low learning rate, and during the reconstruction, we make $M = 2N$ reconstructions with N being the training set size. A full description of our experimental parameters is available in Appendix. To measure reconstruction quality we consider the following metric. We first measure the squared L_2 distance in pixel space from each training image to each reconstruction. We select the pair of training images and reconstruction which has the lowest distance and remove it from the pool, considering it pair of image/reconstruction. We repeat this process until we have a full set of N training images and reconstructions (See Fig. **1**). We then order the L_2 distances into an ascending list of distances and plot this function. We call this the *reconstruction curve* associated with a particular reconstruction set. We plot these reconstruction curves for varying dataset sizes and model widths in Figure **2**. From Figure **2** we have the following three observations:

Smaller training sets are easier to reconstruct. We see that the reconstruction curve for smaller datasets has low values for all model widths. **Wider models can resolve larger datasets.** We observe that for a given model width, there is a threshold image index at which the quality of reconstructions severely decreases. For

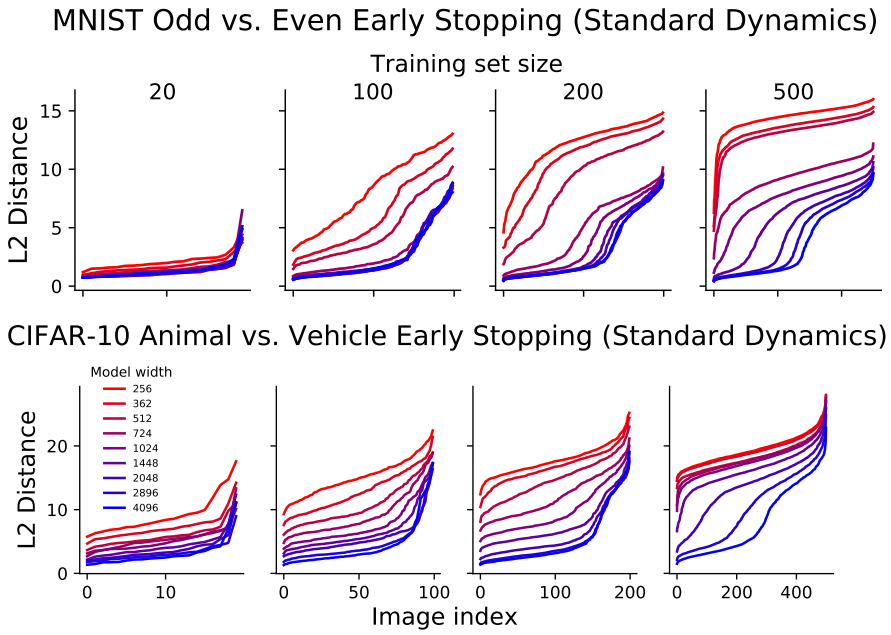

Fig. 4: Reconstruction curves for networks trained to a loss of 1e-2, i.e. significant underfitting (under standard dynamics). Compared to Figure **2**, we see that reconstruction quality is unaffected by early stopping, consistent with the theory.

example, for MNIST Odd/Even, 200 images and a width of 1024, this threshold is 80 images. As we increase the model width this threshold increases almost monotonically.

Linearization improves reconstruction quality. We see that linearized networks can resolve more images and have better images compared to their same-width counterparts. The success of linearization suggests that deviations from the frozen NTK regime affect reconstruction quality. We can measure the deviation from the frozen kernel regime by measuring the *kernel distance* of the network's initialization NTK and its final NTK, given by the following:

$$d(K_0, K_f) = 1 - \frac{\mathrm{Tr}(K_0^\intercal K_f)}{\|K_0\|_F \|K_f\|_F}$$

Intuitively, this distance tells us how well the initialization and final kernel align. Large values indicate that the kernel has changed substantially, meaning the network is deviating far from the NTK regime. We plot these kernel distances against the mean value of the reconstruction curves in figure Figure **3**. We see immediately that reconstruction quality is strongly correlated with kernel distance, and that smaller datasets and wider models have a lower kernel distance.

Early Stopping. In the previous section, we considered models trained with low learning rates for 10^6 epochs, so that we achieve the KKT conditions described in Section 3. In practice, this is computationally expensive, and often ill-advised due to overfitting, with early stopping being a common regularization technique. One major limitation of the attack proposed in Haim et al. (2022) is that it requires the network to reach the KKT point to perform the attack. Our method **does not require the model to reach convergence** for the attack to work. Again we note that the time evolution of network parameters is given by:

Table 1: Performance of KIP, Recon-KIP (RKIP), RKIP with 5% noise pixels, RKIP from a trained network (RKIP-finite), on distilling 500 images down to 20 images. KIP and RKIP provide the best infinite-width performance, while KIP fails for finite models. (n=7)

Distillation Algorithm	MNIST Odd/Even			CIFAR-10 Animal/Vehicle		
	Standard	Linearized	Infinite Width	Standard	Linearized	Infinite Width
Full dataset (500 images)	92.85 ± 0.42	92.91 ± 0.33	93.18 ± 0.37	75.06 ± 0.21	74.60 ± 0.21	75.42 ± 0.28
KIP	57.42 ± 8.41	55.62 ± 7.48	$\mathbf{91.53 \pm 0.57}$	35.26 ± 5.67	32.37 ± 3.60	70.98 ± 0.43
RKIP	$\mathbf{89.61 \pm 1.18}$	$\mathbf{89.99 \pm 1.11}$	91.44 ± 0.48	$\mathbf{72.23 \pm 3.61}$	$\mathbf{72.76 \pm 3.74}$	$\mathbf{74.66 \pm 0.93}$
RKIP 5% noise	86.96 ± 1.37	86.91 ± 1.61	89.66 ± 0.61	70.61 ± 2.14	70.78 ± 2.34	72.56 ± 0.95
RKIP-finite	88.45 ± 0.89	86.15 ± 3.39	87.31 ± 3.24	71.96 ± 1.14	63.99 ± 4.02	62.05 ± 4.17
Random images	73.52 ± 3.60	73.54 ± 3.61	74.12 ± 3.73	70.36 ± 2.53	70.18 ± 2.54	70.77 ± 2.04

$$\Delta\theta(t) = \nabla_\theta f_{\theta_0}(X_T)^\intercal \underbrace{K_0^{-1}\left(I - e^{-\eta K_0 t}\right)\left(y_T - f_{\theta_0}(X_T)\right)}_{\text{time-dependent weights, } \alpha(t)}$$

Notably, even at finite time, the change in network parameters is still a linear combination of the finite-width NTK feature maps of the training set, $\nabla_\theta f_{\theta_0}(X_T)$, with the indicated *time dependent* weights, $\alpha(t)$. Note that the success of the attack in infinite width relies on the injectivity of the kernel measure embedding, not that $\alpha(t)$ be at its converged value, implying the attack works with early stopping. The caveat with the early stopping attack is that we cannot necessarily hope to recover the original training labels.

We verify that this attack works in practice by repeating the attack procedure in Section 4, with early stopping. We apply the attack on networks that achieve a mean training loss of 0.01 (note that this means that on for $\{+1, -1\}$ labels, the outputs were around 0.14 off, i.e. quite underfit), with results shown in Figure **4**. We observe that the attack suffers little to no performance drop, and can sometimes perform better, as there is less time for the kernel to evolve, allowing the network to have *lazier* dynamics.

Multiclass Classification. In previous sections, we showed the validity of the attack on binary classification. Here we verify that the attack works with multiple classes. We repeat the same procedure as in Section 4, but will all 10 classes. Details are given in Appendix. Results are shown by reconstruction curves in Figure **5**. We observe that this attack has **improved** reconstruction quality with more classes. In Section S7.1, we observe that multi-class classification leads to lower kernel distances, suggesting it behaves more in the kernel regimes, explaining the better reconstruction quality. Future work could investigate this further.

5. Unifying Reconstruction and Distillation

In the previous sections, we considered the task of reconstructing the *entire* training set. To do this, we set the reconstruction image count $M > N$. What happens if we set $M < N$? Do we reconstruct a subset of a few training images, or do we form images that are *averages* of the training set in some sense?

We perform this experiment on the CIFAR-10 Animal/Vehicle task with 500 training images for a 4096-width model with linearized dynamics, aiming to reconstruct only 20 images. We recover the images shown in Figure **6**. With a few exceptions, these images are not items of the training set, but rather these images look like *averages* of classes.

Now, what if we retrain a network on these reconstructed images? Noting that the optimal set of dual parameters for a full reconstruction is given by $\alpha^T = K_{TT}^{-1} y_T$, a natural choice for the training labels for these images is

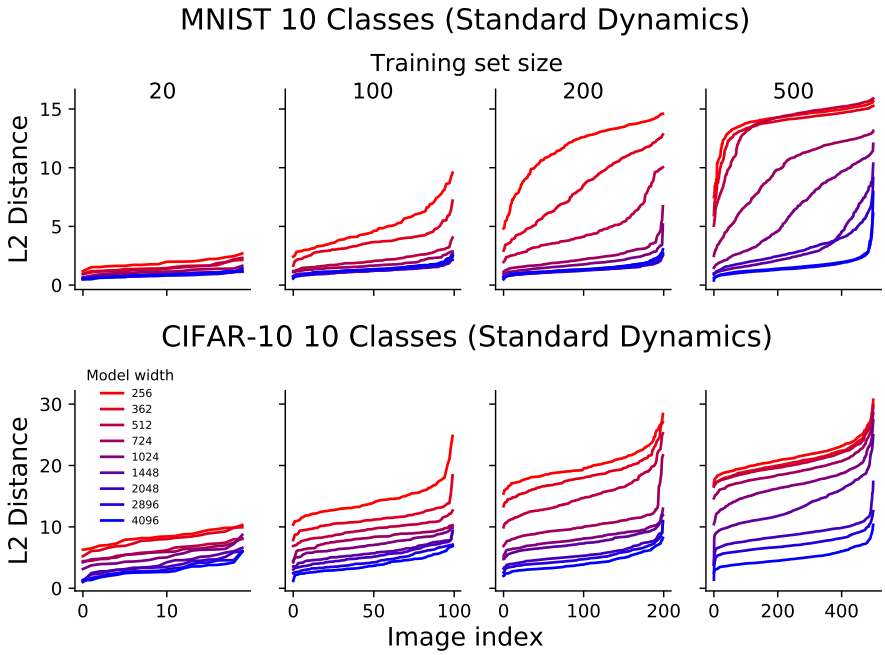

Fig. 5: Reconstruction curves for networks trained on multiclass MNIST/CIFAR-10. The quality improves with more classes.

$y_R = K_{RR}\alpha^R$, where we compute the empirical NTK for K_{RR} and use the learned α^R parameters found during reconstruction. Retraining a different network from scratch on these 20 recovered images yields high accuracy, as shown in Table **1** as RKIP-finite. This suggests that by doing this reconstruction we performed *dataset distillation*, that is we constructed a smaller set of images that accurately approximates the full dataset. This is not a coincidence, and the two algorithms are in fact the same. More formally:

Theorem 2. *The reconstruction scheme outlined in Eq. 4 with KKT points of Eq. 5 and Eq. 6, with $M \leq N$ where M is the reconstruction image counts and N is the dataset size, can be written as a kernel inducing point dataset distillation loss under a different norm plus a variance-controlled error as follows:*

$$\mathcal{L}_{Reconstruction} = \overbrace{\|y_T - K_{TR}K_{RR}^{-1}y_R\|^2_{K_{TT}^{-1}}}^{RKIP\ loss} + \lambda_{var\ of\ R|T}$$

The full proof is given in Section S3. $\lambda_{\text{var of } R|T}$ is proportional to the variance of the reconstruction data points conditioned on the training data, based on the NTK (see Section S3). Intuitively, it ensures that training images provide "information" about the reconstructions. Compared to the loss of a well-known dataset-distillation algorithm, KIP (with S referring to the distilled dataset):

$$\mathcal{L}_{\text{KIP}} = \|y_T - K_{TS}K_{SS}^{-1}y_S\|_2^2$$

The connection is apparent: the reconstruction loss is equal to the KIP dataset distillation loss under a different norm, where, rather than weighting each datapoint equally, we weight training images by their inverse similarity measured by the NTK, plus $\lambda_{\text{var of } r|T}$. This leads to a variant of KIP which we call Recon-KIP (RKIP) which

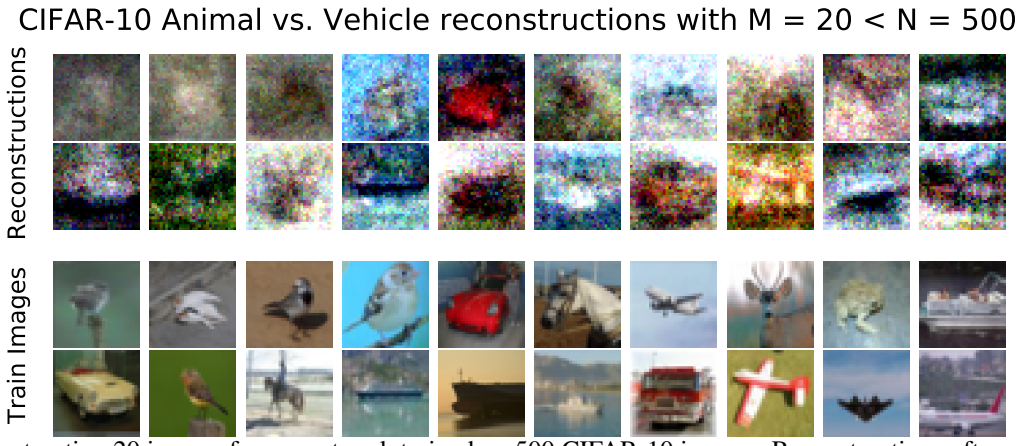

Fig. 6: Reconstructing 20 images from a network trained on 500 CIFAR-10 images. Reconstructions often do not match actual training images and contain heavy corruption. Retraining on these images yields high accuracy.

uses the reconstruction loss in Theorem 2. Note that for large datasets, RKIP is not practically feasible since it requires computing K_{TT}^{-1}, which is typical $N \times N$. We deal with small datasets in this work so it is still tractable.

We summarize the performance on KIP and RKIP in Table **1** on the MNIST Odd/Even and CIFAR-10 Animal/Vehicle task, distilling 500 images down to 20. We evaluate 4096-width networks with standard or linearized dynamics, and infinite width using the NTK. Additionally, we consider using the images/labels made from reconstructing dataset points using a finite network trained on the full dataset (the experiment which led to Figure **6**) and call this RKIP-finite. Note in this case the labels are not necessarily $\{+1, -1\}$, as $K_{0,RR}\alpha^R$ are not guaranteed to be one-hot labels. Similar results for distilling fewer images (20 - 500 training images) to 20 distilled images are shown in figure Figure **9**.

We observe in Table **1** that both KIP and RKIP have high infinite-width accuracies, but KIP sees a significant performance drop when transferring to finite networks. For example, while KIP achieves 91.53% infinite-width test accuracy on the MNIST odd/even task, its finite-width performance is 55.62%, not significantly better than

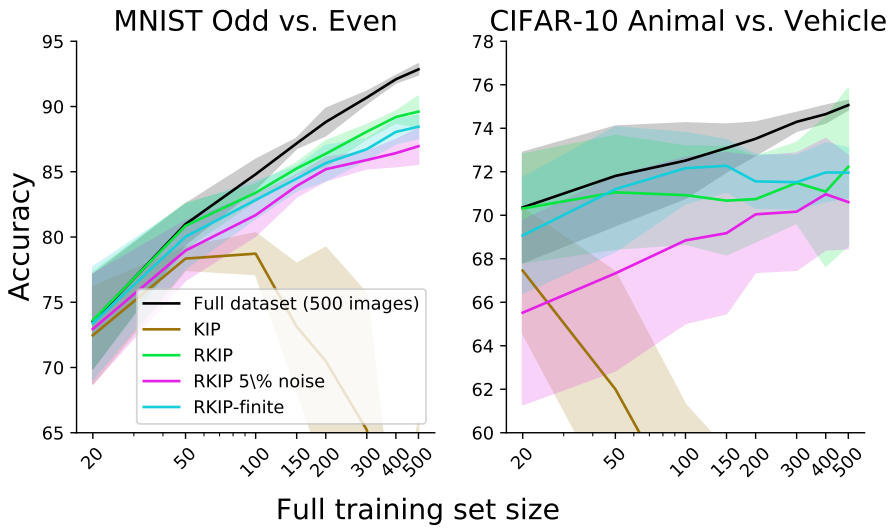

Fig. 7: Performance of KIP, RKIP, RKIP with 5% noise and RKIP-finite on distill N images down to 20 images, trained on a 4096 width network with standard dynamics. KIP fails to transfer to finite networks while RKIP variations succeed.

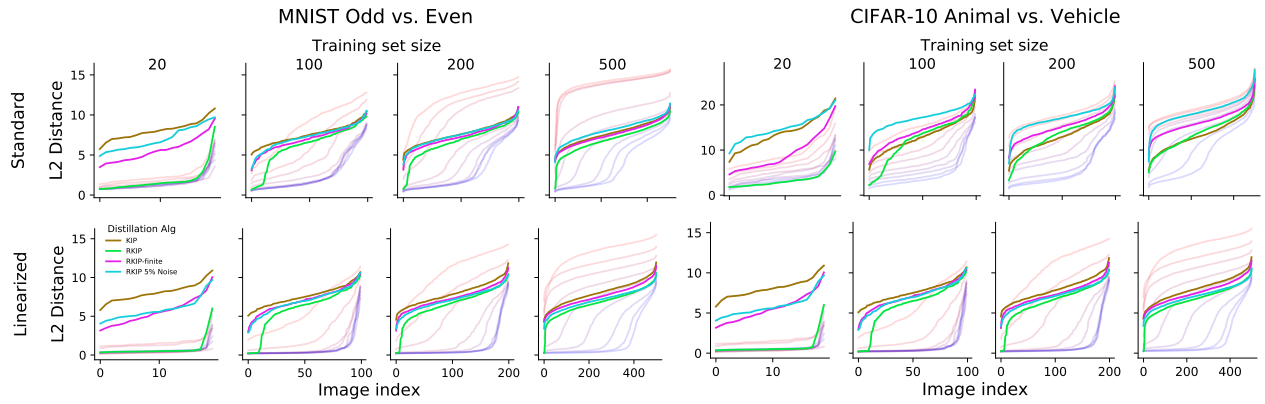

Fig. 8: Reconstruction curves after training on **distilled** images, made with KIP, RKIP, RKIP with 5% noise, or images made from reconstructions (RKIP-finite). We additionally show the reconstruction curves from Figure **2** for comparison. The reconstruction attack is unable to recreate the original training images, except for RKIP, which has a tendency to copy the original training images (see Figure **9**).

a random guess. Interestingly, this performance gap increases as we distill more images, as seen in Figure **7**. For small distilled datasets there is little to no performance drop but for larger ones the difference is significant. In contrast, RKIP surprisingly sees almost no performance drop in the finite-width settings. We hypothesize that this finite-width transfer performance difference for KIP and not RKIP could be due to the contribution of $\lambda_{\text{var of } r|T}$, which we discuss in Section S3. We leave it to future work to explore this further. Note that we use the same training scheme in both scenarios (SGD w/ momentum and low learning rate), and in some preliminary tests we observed that better performance could be achieved by using Adam optimizer for KIP, but we chose to keep the comparison fair and use the same optimizer for all experiments in this paper. Additionally, RKIP-finite performs nearly as well as RKIP, despite distilling using the information from a single finite-width neural network.

6. Defending Against Reconstruction with Distillation

With the connection between reconstruction and distillation established, we next show it is possible to use distillation as a defense against dataset reconstruction attacks. As shown in Section 3, our reconstruction attack is guaranteed to recover the entire training set. A direct implication of this is that if we trained on a different dataset, i.e. a distilled dataset that achieves high performance similar to the original dataset, then this attack will **only recover the distilled dataset**, as any other dataset, notably the original training set, would be suboptimal under the reconstruction loss. If we can ensure that performance is retained through distillation, this could be a viable defense strategy.

To verify this works in practice, we take the same distilled datasets used in Table **1**, trained on 4096-width networks with standard or linearized dynamics, and attempt to reconstruct $2N$ training images (as we did in Section 4). We plot the resulting reconstruction curves in Figure **8**. For KIP, we **fail to reconstruct** the original datasets, however, for RKIP and RKIP-finite this isn't the case. In the 20-image setting, almost all the training images are recovered and even for larger training sets, some of the images are reconstructed well. While at first glance, this seems to be in contradiction to our theory, visualizing the distilled images themselves reveals that RKIP has a strong tendency to recreate some training examples. Since RKIP corresponds to the infinite-width

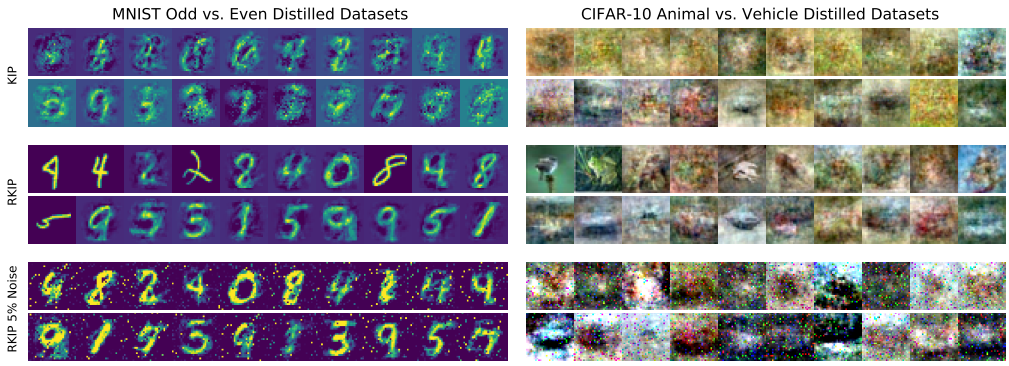

Fig. 9: Visualizations of distilled datasets, on MNIST Odd/Even and CIFAR-10 Animal/Vehicle classification made with KIP, RKIp and RKIP with 5% noise. We distill datasets of 500 original images to 20 images (shown). KIP does not copy the original training images, while RKIP occasionally reproduces training images. Fixing 5% of pixels to be random noise resolves this issue and training images are no longer replicated. Note that distilled data can still resemble training data, but no training image is replicated exactly.

reconstruction attack, when $N_{\text{distilled}} = N_{\text{training}}$, as when $N_{\text{training}} = 20$, RKIP recreates the entire training set, explaining the defense failure in Figure **8**. Surprisingly, KIP does not copy the original training set when $N_{\text{distilled}} = N_{\text{training}}$. We visualize the distilled images when distilling 500 images to 20 images in Figure **9**. We see that even when distilling large datasets, RKIP copies some training examples where KIP does not.

To prevent copying training images, we consider fixing 5% of the distilled images pixels to be random noise, and optimizing only the remaining 95%, following the procedure of KIP_ρ and RFAD_ρ, with ρ, the noise ratio being 0.05. As seen Figure **9**, this prevents exact copying of the training images. Additionally, we see in Figure **8** that this simple procedure now prevents the training images from being reconstructed. From Table **1** and Figure **7**, we see that adding this noise results in only a very minor performance drop, while ensuring that our training images are defended from the reconstruction. Note that this noising procedure does not guarantee differential privacy and is rather primitive. Future work could look at more sophisticated noising schemes which have DP guarantees.

7. Discussion, Limitations, and Conclusion

In this work we showed that a stronger variant of the attack given in Haim et al. (2022) which requires wide neural networks trained under MSE loss can provably reconstruct the entire training set, owing to the injectivity of the NTK kernel measure embedding. We showed that this attack works in practice for finite-width networks, with deviations from the infinite-width regime weakening the attack. Then, we made a novel connection between this reconstruction attack and dataset distillation and finally showed that distillation can defend against this attack, as attackers can only reconstruct the distilled dataset and not the training data. While this sheds light on dataset reconstruction attacks, their theoretical underpinnings, and their defense mechanisms, there are still many avenues to explore.

In this work, we only explored 2-layer fully connected networks, where neural networks are known to behave similarly to their infinite-width counterparts. Meanwhile, deeper convolutional networks are known to deviate significantly, and it is unclear how well the attacks in this paper would transfer to those settings, and what adjustments would need to be made. The study of CNNs and modern deep learning architectures (Hasani et al., 2021, 2022a,b) will be the focus of our continued research. Secondly, while we observed increasing model

width increases the network's "resolving capacity" (i.e. how many images it could reconstruct), future work could look at how this quantity arises from deviations in the finite-width NTK from the infinite width one. Finally, while we showed that we could prevent dataset reconstruction with dataset distillation, we still need to resolve how the dataset reconstruction notion of privacy connects with more established notions such as differential privacy, which is the subject of future work.

Nonetheless, we provide a vital step toward understanding the strengths and weaknesses of dataset reconstruction attacks and provide novel connections to existing literature such as the Neural Tangent Kernel and dataset distillation.

Acknowledgments

This research was supported in part by the AI2050 program at Schmidt Futures (Grant G-22-63172), the Boeing Company, and the United States Air Force Research Laboratory and the United States Air Force Artificial Intelligence Accelerator and was accomplished under Cooperative Agreement Number FA8750-19-2-1000. The views and conclusions contained in this document are those of the authors and should not be interpreted as representing the official policies, either expressed or implied, of the United States Air Force or the U.S. Government. The U.S. Government is authorized to reproduce and distribute reprints for Government purposes, notwithstanding any copyright notation herein. This work was further supported by The Boeing Company and Office of Naval Research grant N00014-18-1-2830, DSTA Singapore, and the J. P. Morgan AI Research program. We are very grateful.

References

M. Abadi, A. Chu, I. Goodfellow, H. B. McMahan, I. Mironov, K. Talwar, and L. Zhang. Deep learning with differential privacy. In *Proceedings of the 2016 ACM SIGSAC Conference on Computer and Communications Security*, CCS '16, page 308–318, New York, NY, USA, 2016. Association for Computing Machinery. ISBN 9781450341394. doi: 10.1145/2976749.2978318. URL https://doi.org/10.1145/2976749.2978318.

K. Aitken and G. Gur-Ari. On the asymptotics of wide networks with polynomial activations. *ArXiv*, abs/2006.06687, 2020.

S. Arora, S. S. Du, W. Hu, Z. Li, R. R. Salakhutdinov, and R. Wang. On exact computation with an infinitely wide neural net. In *Advances in Neural Information Processing Systems*, pages 8141–8150. Curran Associates, Inc., 2019.

D. Arpit, S. Jastrzebski, N. Ballas, D. Krueger, E. Bengio, M. S. Kanwal, T. Maharaj, A. Fischer, A. Courville, Y. Bengio, et al. A closer look at memorization in deep networks. In *International conference on machine learning*, pages 233–242. PMLR, 2017.

I. Babuschkin, K. Baumli, A. Bell, S. Bhupatiraju, J. Bruce, P. Buchlovsky, D. Budden, T. Cai, A. Clark, I. Danihelka, C. Fantacci, J. Godwin, C. Jones, R. Hemsley, T. Hennigan, M. Hessel, S. Hou, S. Kapturowski, T. Keck, I. Kemaev, M. King, M. Kunesch, L. Martens, H. Merzic, V. Mikulik, T. Norman, J. Quan, G. Papamakarios, R. Ring, F. Ruiz, A. Sanchez, R. Schneider, E. Sezener, S. Spencer, S. Srinivasan, L. Wang, W. Stokowiec, and F. Viola. The DeepMind JAX Ecosystem, 2020. URL http://github.com/deepmind.

L. Bourtoule, V. Chandrasekaran, C. A. Choquette-Choo, H. Jia, A. Travers, B. Zhang, D. Lie, and N. Papernot. Machine unlearning. *CoRR*, abs/1912.03817, 2019. URL http://arxiv.org/abs/1912.03817.

J. Bradbury, R. Frostig, P. Hawkins, M. J. Johnson, C. Leary, D. Maclaurin, G. Necula, A. Paszke, J. VanderPlas, S. Wanderman-Milne, and Q. Zhang. JAX: composable transformations of Python+NumPy programs, 2018. URL http://github.com/google/jax.

G. Brown, M. Bun, V. Feldman, A. Smith, and K. Talwar. When is memorization of irrelevant training data necessary for high-accuracy learning? In *Proceedings of the 53rd Annual ACM SIGACT Symposium on Theory of Computing*, pages 123–132, 2021.

N. Carlini, C. Liu, U. Erlingsson, J. Kos, and D. Song. The secret sharer: Evaluating and testing unintended memorization in neural networks. In *Proceedings of the 28th USENIX Conference on Security Symposium*, SEC'19, page 267–284, USA, 2019. USENIX Association. ISBN 9781939133069.

Centers for Medicare & Medicaid Services. The Health Insurance Portability and Accountability Act of 1996 (HIPAA). Online at http://www.cms.hhs.gov/hipaa/, 1996.

L. Chizat, E. Oyallon, and F. R. Bach. On lazy training in differentiable programming. In *NeurIPS*, 2019.

R. de Azevedo. Does gradient descent converge to a minimum-norm solution in least-squares problems? Mathematics Stack Exchange. URL https://math.stackexchange.com/q/3499305. URL:https://math.stackexchange.com/q/3499305 (version: 2022-02-18).

C. Dwork, F. McSherry, K. Nissim, and A. Smith. Calibrating noise to sensitivity in private data analysis. In *Proceedings of the Third Conference on Theory of Cryptography*, TCC'06, page 265–284, Berlin, Heidelberg, 2006. Springer-Verlag. ISBN 3540327312. doi: 10.1007/11681878_14. URL https://doi.org/10.1007/11681878_14.

European Commission. Regulation (EU) 2016/679 of the European Parliament and of the Council of 27 April 2016 on the protection of natural persons with regard to the processing of personal data and on the free movement of such data, and repealing Directive 95/46/EC (General Data Protection Regulation) (Text with EEA relevance), 2016. URL https://eur-lex.europa.eu/eli/reg/2016/679/oj.

V. Feldman. Does learning require memorization? a short tale about a long tail. In *Proceedings of the 52nd Annual ACM SIGACT Symposium on Theory of Computing*, STOC 2020, page 954–959, New York, NY, USA, 2020. Association for Computing Machinery. ISBN 9781450369794. doi: 10.1145/3357713.3384290. URL https://doi.org/10.1145/3357713.3384290.

V. Feldman and C. Zhang. What neural networks memorize and why: Discovering the long tail via influence estimation. In *Proceedings of the 34th International Conference on Neural Information Processing Systems*, NIPS'20, Red Hook, NY, USA, 2020. Curran Associates Inc. ISBN 9781713829546.

S. Fort, G. K. Dziugaite, M. Paul, S. Kharaghani, D. M. Roy, and S. Ganguli. Deep learning versus kernel learning: an empirical study of loss landscape geometry and the time evolution of the neural tangent kernel. In *NeurIPS*, 2020. URL https://proceedings.neurips.cc/paper/2020/hash/405075699f065e43581f27d67bb68478-Abstract.html.

M. Fredrikson, S. Jha, and T. Ristenpart. Model inversion attacks that exploit confidence information and basic countermeasures. In *Proceedings of the 22nd ACM SIGSAC conference on computer and communications security*, pages 1322–1333, 2015.

A. Gretton, K. M. Borgwardt, M. J. Rasch, B. Schölkopf, and A. Smola. A kernel two-sample test. *J. Mach. Learn. Res.*, 13(null):723–773, mar 2012. ISSN 1532-4435.

S. A. Gruenbacher, M. Lechner, R. Hasani, D. Rus, T. A. Henzinger, S. A. Smolka, and R. Grosu. Gotube: Scalable statistical verification of continuous-depth models. In *Proceedings of the AAAI Conference on Artificial Intelligence*, volume 36, pages 6755–6764, 2022.

S. Grunbacher, R. Hasani, M. Lechner, J. Cyranka, S. A. Smolka, and R. Grosu. On the verification of neural odes with stochastic guarantees. In *Proceedings of the AAAI Conference on Artificial Intelligence*, volume 35, pages 11525–11535, 2021.

N. Haim, G. Vardi, G. Yehudai, michal Irani, and O. Shamir. Reconstructing training data from trained neural networks. In A. H. Oh, A. Agarwal, D. Belgrave, and K. Cho, editors, *Advances in Neural Information Processing Systems*, 2022. URL https://openreview.net/forum?id=Sxk8Bse3RKO.

B. Hanin and M. Nica. Finite depth and width corrections to the neural tangent kernel. In *International Conference on Learning Representations*, 2020. URL https://openreview.net/forum?id=SJgndT4KwB.

R. Hasani, M. Lechner, A. Amini, D. Rus, and R. Grosu. Liquid time-constant networks. In *Proceedings of the AAAI Conference on Artificial Intelligence*, volume 35, pages 7657–7666, 2021.

R. Hasani, M. Lechner, A. Amini, L. Liebenwein, A. Ray, M. Tschaikowski, G. Teschl, and D. Rus. Closed-form continuous-time neural networks. *Nature Machine Intelligence*, pages 1–12, 2022a.

R. Hasani, M. Lechner, T.-H. Wang, M. Chahine, A. Amini, and D. Rus. Liquid structural state-space models. *arXiv preprint arXiv:2209.12951*, 2022b.

Z. He, T. Zhang, and R. B. Lee. Model inversion attacks against collaborative inference. In *Proceedings of the 35th Annual Computer Security Applications Conference*, ACSAC '19, page 148–162, New York, NY, USA, 2019. Association for Computing Machinery. ISBN 9781450376280. doi: 10.1145/3359789.3359824. URL https://doi.org/10.1145/3359789.3359824.

J. Heek, A. Levskaya, A. Oliver, M. Ritter, B. Rondepierre, A. Steiner, and M. van Zee. Flax: A neural network library and ecosystem for JAX, 2020. URL http://github.com/google/flax.

A. Jacot, F. Gabriel, and C. Hongler. Neural tangent kernel: Convergence and generalization in neural networks. In S. Bengio, H. Wallach, H. Larochelle, K. Grauman, N. Cesa-Bianchi, and R. Garnett, editors, *Advances in Neural Information Processing Systems*, volume 31. Curran Associates, Inc., 2018. URL https://proceedings.neurips.cc/paper/2018/file/5a4be1fa34e62bb8a6ec6b91d2462f5a-Paper.pdf.

Z. Ji and M. Telgarsky. Directional convergence and alignment in deep learning. In H. Larochelle, M. Ranzato, R. Hadsell, M. Balcan, and H. Lin, editors, *Advances in Neural Information Processing Systems*, volume 33, pages 17176–17186. Curran Associates, Inc., 2020. URL https://proceedings.neurips.cc/paper/2020/file/c76e4b2fa54f8506719a5c0dc14c2eb9-Paper.pdf.

D. P. Kingma and J. Ba. Adam: A method for stochastic optimization. In Y. Bengio and Y. LeCun, editors, *3rd International Conference on Learning Representations, ICLR 2015, San Diego, CA, USA, May 7-9, 2015, Conference Track Proceedings*, 2015. URL http://arxiv.org/abs/1412.6980.

P. W. Koh and P. Liang. Understanding black-box predictions via influence functions. In *Proceedings of the 34th International Conference on Machine Learning - Volume 70*, ICML'17, page 1885–1894. JMLR.org, 2017.

M. Lechner, R. Hasani, A. Amini, T. A. Henzinger, D. Rus, and R. Grosu. Neural circuit policies enabling auditable autonomy. *Nature Machine Intelligence*, 2(10):642–652, 2020.

M. Lechner, R. Hasani, R. Grosu, D. Rus, and T. A. Henzinger. Adversarial training is not ready for robot learning. In *2021 IEEE International Conference on Robotics and Automation (ICRA)*, pages 4140–4147. IEEE, 2021.

J. Lee, L. Xiao, S. Schoenholz, Y. Bahri, R. Novak, J. Sohl-Dickstein, and J. Pennington. Wide neural networks of any depth evolve as linear models under gradient descent. *Advances in neural information processing systems*, 32, 2019.

N. Loo, R. Hasani, A. Amini, and D. Rus. Efficient dataset distillation using random feature approximation. *Advances in Neural Information Processing Systems*, 2022a.

N. Loo, R. Hasani, A. Amini, and D. Rus. Evolution of neural tangent kernels under benign and adversarial training. In *Advances in Neural Information Processing Systems*, 2022b.

K. Lyu and J. Li. Gradient descent maximizes the margin of homogeneous neural networks. In *International Conference on Learning Representations*, 2020. URL https://openreview.net/forum?id=SJeLIgBKPS.

T. Nguyen, Z. Chen, and J. Lee. Dataset meta-learning from kernel ridge-regression. In *International Conference on Learning Representations*, 2021a. URL https://openreview.net/forum?id=l-PrrQrK0QR.

T. Nguyen, R. Novak, L. Xiao, and J. Lee. Dataset distillation with infinitely wide convolutional networks. In *Thirty-Fifth Conference on Neural Information Processing Systems*, 2021b. URL https://openreview.net/forum?id=hXWPpJedrVP.

R. Novak, L. Xiao, J. Hron, J. Lee, A. A. Alemi, J. Sohl-Dickstein, and S. S. Schoenholz. Neural tangents: Fast and easy infinite neural networks in python. In *International Conference on Learning Representations*, 2020. URL https://openreview.net/forum?id=SklD9yrFPS.

R. Novak, J. Sohl-Dickstein, and S. S. Schoenholz. Fast finite width neural tangent kernel. In K. Chaudhuri, S. Jegelka, L. Song, C. Szepesvári, G. Niu, and S. Sabato, editors, *International Conference on Machine Learning, ICML 2022, 17-23 July 2022, Baltimore, Maryland, USA*, volume 162 of *Proceedings of Machine Learning Research*, pages 17018–17044. PMLR, 2022. URL https://proceedings.mlr.press/v162/novak22a.html.

M. Rigaki and S. Garcia. A survey of privacy attacks in machine learning. *CoRR*, abs/2007.07646, 2020. URL https://arxiv.org/abs/2007.07646.

R. Shokri, M. Stronati, and V. Shmatikov. Membership inference attacks against machine learning models. *CoRR*, abs/1610.05820, 2016. URL http://arxiv.org/abs/1610.05820.

B. K. Sriperumbudur, K. Fukumizu, and G. R. Lanckriet. Universality, characteristic kernels and rkhs embedding of measures. *Journal of Machine Learning Research*, 12(70):2389–2410, 2011. URL http://jmlr.org/papers/v12/sriperumbudur11a.html.

N. Tsilivis and J. Kempe. What can the neural tangent kernel tell us about adversarial robustness? In A. H. Oh, A. Agarwal, D. Belgrave, and K. Cho, editors, *Advances in Neural Information Processing Systems*, 2022. URL https://openreview.net/forum?id=KBUgVv8z7OA.

T. Wang, J.-Y. Zhu, A. Torralba, and A. A. Efros. Dataset distillation. *arXiv preprint arXiv:1811.10959*, 2018.

W. Xiao, R. Hasani, X. Li, and D. Rus. Barriernet: A safety-guaranteed layer for neural networks. *arXiv preprint arXiv:2111.11277*, 2021.

W. Xiao, T.-H. Wang, R. Hasani, M. Lechner, and D. Rus. On the forward invariance of neural odes. *arXiv preprint arXiv:2210.04763*, 2022.

Z. Yang, J. Zhang, E.-C. Chang, and Z. Liang. Neural network inversion in adversarial setting via background knowledge alignment. In *Proceedings of the 2019 ACM SIGSAC Conference on Computer and Communications Security*, CCS '19, page 225–240, New York, NY, USA, 2019. Association for Computing Machinery. ISBN 9781450367479. doi: 10.1145/3319535.3354261. URL https://doi.org/10.1145/3319535.3354261.

A. Zandieh, I. Han, H. Avron, N. Shoham, C. Kim, and J. Shin. Scaling neural tangent kernels via sketching and random features. In A. Beygelzimer, Y. Dauphin, P. Liang, and J. W. Vaughan, editors, *Advances in Neural Information Processing Systems*, 2021. URL https://openreview.net/forum?id=vIRFiA658rh.

C. Zhang, S. Bengio, M. Hardt, B. Recht, and O. Vinyals. Understanding deep learning requires rethinking generalization. In *International Conference on Learning Representations*, 2017. URL https://openreview.net/forum?id=Sy8gdB9xx.

C. Zhang, S. Bengio, M. Hardt, B. Recht, and O. Vinyals. Understanding deep learning (still) requires rethinking generalization. *Commun. ACM*, 64(3):107–115, feb 2021. ISSN 0001-0782. doi: 10.1145/3446776. URL https://doi.org/10.1145/3446776.

B. Zhao and H. Bilen. Dataset condensation with differentiable siamese augmentation. *arXiv preprint arXiv:2102.08259*, 2021.

B. Zhao, K. R. Mopuri, and H. Bilen. Dataset condensation with gradient matching. In *International Conference on Learning Representations*, 2021. URL https://openreview.net/forum?id=mSAKhLYLSsl.

Y. Zhou, E. Nezhadarya, and J. Ba. Dataset distillation using neural feature regression. In *Proceedings of the Advances in Neural Information Processing Systems (NeurIPS)*, 2022.

L. Zhu, Z. Liu, , and S. Han. Deep leakage from gradients. In *Annual Conference on Neural Information Processing Systems (NeurIPS)*, 2019.

Supplementary Materials

S1. Comparison to Haim et al. (2022)

In Section 3, we mentioned that we had problems reproducing Haim et al. (2022)'s attack. Here, we compare the two attacks and discuss the issues we found with theirs.

Firstly, we compare the quality of the two attacks. Haim et al. (2022) open-sourced their code, and gave the best two sets of reconstructions for both CIFAR-10 and MNIST-10. We plot the reconstruction curves of these reconstructions here:

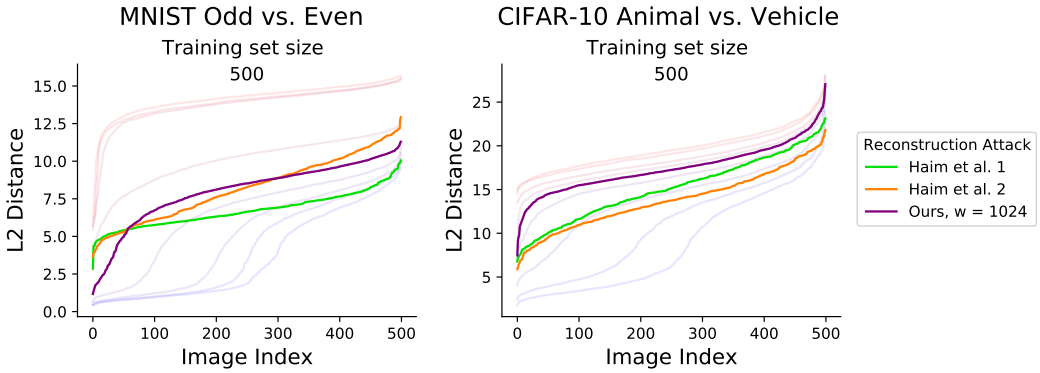

Fig. S1: Reconstruction curves for the attacks given in Haim et al. (2022), in comparison to our reconstruction attacks, with a comparable width of 1024.

In their paper, they consider networks of a width 1000, so for a fair comparison, we highlight our reconstruction with a comparable width of 1024, under standard dynamics. We see that for MNIST, our attack has significantly better quality until image index 50 in which case both attacks perform poorly. For CIFAR-10, our attack performs worse but can achieve better performance with wider width or linearization.

Note that the two reconstruction curves presented from Haim et al. (2022) correspond to the two *best* reconstructions with carefully chosen hyperparameters. These hyperparameters are chosen to maximize reconstruction quality, which requires access to the training data to measure the quality. A priori, an attacker would not be able to assess reconstruction quality, and thus would not be able to do such hyperparameter tuning. In contrast, attack parameters such as learning rate/initialization were not fine-tuned for ours, and we use the same hyperparameters for every attack. Further gains could likely be seen with more careful tuning. We would like to emphasize that the goal of this work is not necessarily to create the strongest attack, but more so to explore the properties of the attack, and conditions for failure/success.

A further limitation of their attack is that it requires homogenous neural networks (i.e. no biases), in comparison to ours which uses biases, which is closer to practice. The largest limitation of their attack is that they require **a careful initialization scheme**, in which the weights of the first layer are initialized with significantly smaller variance. In Haim et al. (2022) they discuss that this is **essential** to the success of their attack. In contrast, we use the default initialization given in the Flax neural network library (Heek et al., 2020).

We also observed that the KKT condition given in Equation (1), which is required for their attack to work often is not reached in practice. To reiterate the definition of directional convergence, it requires that $\lim_{t\to\infty} \frac{\theta}{\|\theta\|_2} \to \frac{\theta'}{\|\theta'\|_2}$ for trained network parameters θ, and θ' the solution to Equation (1). It is clear that if $\frac{\|\theta-\theta_0\|_2^2}{\|\theta_0\|_2^2} < 1$, i.e. the parameters have not drifted far from their initialization, then, we cannot hope the KKT point is reached (of

course, with unlikely exceptions such as θ_0 already being close to the KKT point). In practice, we found that $\|\theta_0\|_2^2 \approx 333$ and $\|\theta\|_2^2 \approx 377$, when running their attack, which suggests that the initialization still contributes a significant amount to the final parameters, suggesting that the KKT was not reached. Of course, our attack is not without limitations as well, the most notable being that we require network initialization. We leave it to future work to alleviate this requirement.

S2. Label conditions for full recovery

As discussed in Section 3, we require that $\alpha_i \neq 0$ in order to recover the training image. Here we discuss the conditions for this to occur. We know that $\alpha = K^{-1}y$, and without loss of generality, consider reconstructing the final image at index N. Our equation for α becomes, focusing on the value of α_N:

$$\begin{bmatrix} \alpha_{:N-1} \\ \alpha_N \end{bmatrix} = \begin{bmatrix} K_{:N-1,:N-1} & K_{:N-1,:N} \\ K_{:N-1,:N}^\intercal & K_{N,N} \end{bmatrix}^{-1} \begin{bmatrix} y_{:N-1} \\ y_N \end{bmatrix}$$
$$\begin{bmatrix} \alpha_{:N-1} \\ \alpha_N \end{bmatrix} = \begin{bmatrix} K_{:N-1,:N-1}^{-1} + K_{:N-1,:N-1}^{-1} K_{:N-1,:N} Q K_{:N-1,:N}^\intercal K_{:N-1,:N-1}^{-1} & -K_{:N-1,:N-1}^{-1} K_{:N-1,:N} Q \\ -Q K_{:N-1,:N}^T K_{:N-1,:N-1}^{-1} & Q \end{bmatrix} \begin{bmatrix} y_{:N-1} \\ y_N \end{bmatrix}$$

With $Q = (K_{N,N} - K_{:N-1,:N} K_{:N-1,:N-1}^{-1} K_{:N-1,:N}^\intercal)^{-1}$. Setting $\alpha_N = 0$:

$$0 = -Q K_{:N-1,:N}^T K_{:N-1,:N-1}^{-1} y_{:N-1} + Q y_N$$
$$y_N = K_{:N-1,:N}^T K_{:N-1,:N-1}^{-1} y_{:N-1}$$

Noting $K_{:N-1,:N}^T K_{:N-1,:N-1}^{-1} y_{:N-1}$ corresponds to the kernel regression prediction of y_N given $y_{:N-1}$, we see that $\alpha_N = 0$ iff x_N is already perfectly predicted by the remaining data points. Of course, the label corresponding exactly to the prediction occurs with probability 0.

S3. Proof of Theorem 5.1: RKIP Derivation from Reconstruction loss

Proof. Here we derive how one gets from the reconstruction loss given in Equation (7) to Theorem 2, the RKIP loss. We repeat the losses here:

$$\mathcal{L}_{\text{Reconstruction}} = \|\Delta\theta - \alpha^\intercal \nabla_\theta f_{\theta_0}(X_T)\|_2^2$$
$$\mathcal{L}_{\text{RKIP}} = \|y_T - K_{TR} K_{RR}^{-1} y_R\|_{K_{TT}^{-1}}^2$$

First we note that $\alpha^T = K_{TT}^{-1} y_T$, and if we trained on reconstructions with labels y_R, then $\alpha^R = K_{RR}^{-1} y_R$. For brevity we denote $s_i^* = \{\alpha_i^*, x_i^*\}$ and $S^* = \{\alpha^*, X_*\}$. Let S^T and S^R denote the training and reconstruction

set, respectively

$$\begin{aligned}
&\left\|\Delta\theta - \sum_{s_j^R \in S^R} \alpha_j^R \nabla_{\theta_f} f_{\theta_f}(x_j^R)\right\|_2^2 \\
&= \left\|\sum_{s_i^T \in S^T} \alpha_i^T \nabla_{\theta_0} f(x_i^T) - \sum_{s_j^R \in S_R} \alpha_j^R \nabla_{\theta_f} f_{\theta_f}(x_j^R)\right\|_2^2 \\
&= \left\|\sum_{s_i^T \in S^T} \alpha_i^T k_{\theta_0}(x_i^T, \cdot) - \sum_{s_j^R \in S_R} \alpha_j^R k_{\theta_f}(x_j^R, \cdot)\right\|_2^2
\end{aligned}$$

Again take the infinite width limit so $k_{\theta_0}, k_{\theta_f} \to k_{NTK}$, we which just write k for simplicity.

$$\begin{aligned}
\left\|\sum_{s_i^T \in S^T} \alpha_i^T k_{\theta_0}(x_i^T, \cdot) - \sum_{s_j^R \in S_R} \alpha_j^R k_{\theta_f}(x_j^R, \cdot)\right\|_2^2 &\to \left\|\sum_{s_i^T \in S^T} \alpha_i^T k(x_i^T, \cdot) - \sum_{s_j^R \in S_R} \alpha_j^R k(x_j^R, \cdot)\right\|_2^2 \\
&= \sum_{s_i^T \in S^T} \sum_{s_j^T \in S^T} \alpha_i^T \alpha_j^T k(x_i^T, x_j^T) - 2 \sum_{s_i^T \in S^T} \sum_{s_j^R \in S^R} \alpha_i^T \alpha_j^R k(x_i^T, x_j^R) \\
&\quad + \sum_{s_i^R \in S^R} \sum_{s_j^R \in S^R} \alpha_i^R \alpha_j^R k(x_i^R, x_j^R) \\
&= \alpha^{T\intercal} K_{TT} \alpha^T - 2\alpha^{T\intercal} K_{TR} \alpha^R + \alpha^{R\intercal} K_{RR} \alpha^R \\
&= y_T^\intercal K_{TT}^{-1} K_{TT} K_{TT}^{-1} y_T - 2 y_T^\intercal K_{TT}^{-1} K_{TR} K_{RR}^{-1} y_R + y_R^\intercal K_{RR}^{-1} K_{RR} K_{RR}^{-1} y_R \\
&= y_T^\intercal K_{TT}^{-1} y_T - 2 y_T^\intercal K_{TT}^{-1} K_{TR} K_{RR}^{-1} y_R + y_R^\intercal K_{RR}^{-1} y_R \\
&= y_T^\intercal K_{TT}^{-1} y_T - 2 y_T^\intercal K_{TT}^{-1} K_{TR} K_{RR}^{-1} y_R + y_R^\intercal K_{RR}^{-1} K_{RT} K_{TT}^{-1} K_{TR} K_{RR}^{-1} y_R \\
&\quad - y_R^\intercal K_{RR}^{-1} K_{RT} K_{TT}^{-1} K_{TR} K_{RR}^{-1} y_R + y_R^\intercal K_{RR}^{-1} y_R \\
&= \|y_T - K_{TR} K_{RR}^{-1} y_R\|_{K_{TT}^{-1}}^2 + y_R^\intercal (K_{RR}^{-1} - K_{RR}^{-1} K_{RT} K_{TT}^{-1} K_{TR} K_{RR}^{-1}) y_R \\
&= \underbrace{\|y_T - K_{TR} K_{RR}^{-1} y_R\|_{K_{TT}^{-1}}^2}_{\text{label matching}} + \underbrace{y_R^\intercal K_{RR}^{-1} (K_{RR} - K_{RT} K_{TT}^{-1} K_{TR}) K_{RR}^{-1} y_R}_{\lambda_{\text{var of } R|T}}
\end{aligned}$$

□

$\lambda_{\text{var of } R|T}$ is proportional to $K_{RR} - K_{RT} K_{TT}^{-1} K_{TR}$, which is $K_{[T,R],[T,R]} / K_{TT}$, the Schur complement of $K_{[T,R],[T,R]}$ with K_{TT}. Note that this is the Gaussian conditional variance formula, assuming we are making predictions of R based on T. This regularizer ensures that not only do the reconstructed images result in the correct predictions (ensured by the label matching term) but also that our distilled dataset images do not deviate significantly from the training distribution, as measured by the NTK. We hypothesize this term is what contributes to the success of RKIP over KIP in the finite-width setting. As there is nothing that directly ensures that KIP distilled datapoints remain "similar" to training images (only that they are predictive), these distilled images may be more susceptible to domain shift, such as moving from the infinite-width setting to finite width. This interesting behavior could be the subject of future work.

S4. Multiclass Reconstruction Loss

Here we derive the multi-class reconstruction loss which we use in Section 4. Our least-norm predictor satisfies the following conditioned (assuming that the network behaves in the linear regime):

$$\begin{aligned} &\underset{\Delta\theta}{\operatorname{argmin}} \frac{1}{2}\|\Delta\theta\|_2^2 \quad s.t. \\ &\forall c \in [C], \quad \Delta\theta^\intercal \nabla_\theta f^c_{\theta_0}(X_T) = y^c_T - f^c_{\theta_0}(X_T). \end{aligned} \tag{S1}$$

With $f^c_{\theta_0}$ referring to the network output on the cth class and y^c_T referring to the training labels for the cth class. The network will converge to the least norm solution (norm of the difference from initialization), due to the network behaving in the lazy regime with gradient flow (de Azevedo). Writing the equation with dual variables our full Lagrangian is

$$\mathcal{L}(\Delta\theta, \alpha) = \frac{1}{2}\|\Delta\theta\|_2^2 + \sum_{c=1}^{C} \alpha^{c\intercal} \left(\Delta\theta^\intercal \nabla_\theta f^c_{\theta_0}(X_T) - (y^c_T - f^c_{\theta_0}(X_T))\right). \tag{S2}$$

With α our set of dual parameters $\in R^{C\times M}$, that is, we have a set of M dual parameters for each class. Taking derives w.r.t $\Delta\theta$:

$$0 = \nabla_{\Delta\theta}\mathcal{L}(\Delta\theta, \alpha) = \Delta\theta + \sum_{c=1}^{C} \alpha^{c\intercal} \left(\nabla_\theta f^c_{\theta_0}(X_T)\right). \tag{S3}$$

So our multiclass reconstruction loss is

$$\mathcal{L}_{\text{reconstrution}} = \left\| \Delta\theta - \sum_{c=1}^{C} \alpha^{c\intercal} \nabla_\theta f^c_{\theta_0}(X_T) \right\|_2^2. \tag{S4}$$

We can use the same argument as in Section 3 to show this attack is exact in the infinite width limit.

S5. Experimental Details

S5.1. Libraries and Hardware

We use the JAX, Optax, Flax, and neural-tangents libraries (Babuschkin et al., 2020; Bradbury et al., 2018; Heek et al., 2020; Novak et al., 2020, 2022). All experiments were run on NVidia Titan RTX graphics cards with 24Gb VRAM.

S5.2. Network training

Unless otherwise stated, networks trained on real data are trained for 10^6 iterations of full batch gradient descent, with SGD with momentum 0.9. For the learning rate, we set $\eta = N \times 2\text{e}{-7}$, where N is the number

of training images. For distilled data, we use a learning rate of $\eta = N \times 6\text{e}{-6}$, where N is now the distilled dataset size. We did not find that results were heavily dependent on the learning rates used during training. Additionally, if the training loss was less than $1\text{e}{-10}$, we terminated training early. Every reconstruction curve in the main text is the average of 3 unique networks trained on 3 unique splits of training data.

For binary classification, we use labels in $\{+1, -2\}$, and for 10-way multiclass classification, we use labels of 0.9 corresponding to the selected class and -0.1 for other classes.

S5.3. Reconstructions

To create reconstructions, we initialize reconstruction images with a standard deviation of 0.2, and dual parameters to be uniform random within $[-0.5, 0.5]$. We use Adam optimizer (Kingma and Ba, 2015), with a learning rate of 0.02 for all reconstructions. As stated in Section S1, these could be fine-tuned to improve performance. We optimize the images for 80k iterations. Like with Haim et al. (2022), we found that it was useful to use a `softplus` rather than a `ReLu` during reconstruction, owing to the smoothing gradient loss. We annealed `softplus` temperature from 10 to 200 over the course of training, so that we are effectively using `ReLUs` by the end of training. Unless otherwise stated, we aim to reconstruct $M = 2N$ reconstruction images, with N the training set size.

S5.4. Distillation

We initialize distilled images with a standard deviation of 0.2 and distill for 50k iterations with Adam optimizer with a learning rate of 0.001.

S6. Reconstruction Post-Processing

We do not post-process our reconstructions and the reconstruction curves and visualization are based on unmodified reconstructions. Note that Haim et al. (2022) has a more complex reconstruction scheme involving rescaling the reconstructions and averaging, which is detailed in Haim et al. (2022)'s appendix.

S7. Additional Results

S7.1. Kernel Distance vs. Reconstruction Quality Scatter plots for Multiclass Classifications

Figure S2 shows the corresponding Figure **3** for multiclass classification. As we observed, multiclass classification has improved reconstruction quality. From Figure S2, we see that multiclass classification sees significantly lower kernel distances (up to 1e-2 for MNIST and 2e-2 for CIFAR-10) compared to binary classification (up to 3e-2 for MNIST and 9e-2 for CIFAR-10, see Figure **3**), which may explain why the reconstructions have better quality.

S7.2. Additional Reconstruction Curves

We show additional reconstruction curves for all dataset sizes in $[20, 50, 100, 150, 200, 300, 400, 500]$ for MNIST Odd vs. Even and CIFAR-10 Animal vs. Vehicle in Figure S3. We show the same reconstruction curves with

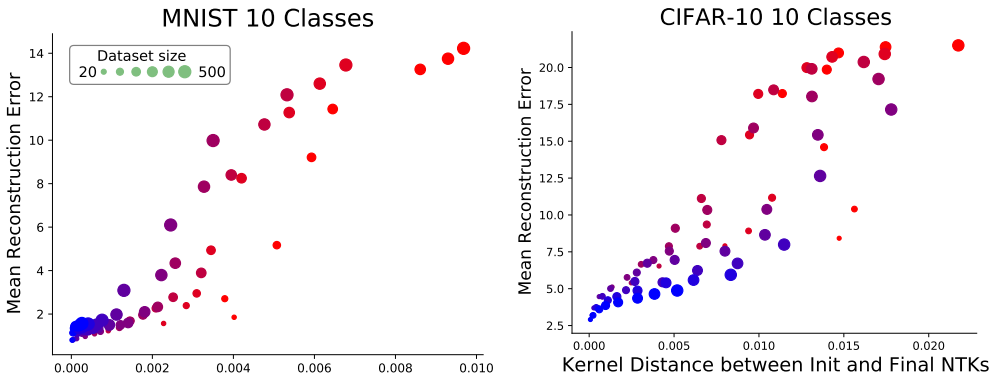

Fig. S2: Mean reconstruction error vs. the kernel distance from the initialization kernel to the final kernel for multiclass classification. The mean reconstruction error, measured as the average value of the reconstruction curve, is strongly correlated with how much the finite-width NTK evolves over training. Dataset size is given by dot size, while the color indicates model width. Multiclass classification sees significantly lower kernel distances (up to 1e-2 for MNIST and 2e-2 for CIFAR-10) compared to binary classification (up to 3e-2 for MNIST and 9e-2 for CIFAR-10, see Figure **3**), which may be the cause of better reconstruction quality.

.

the distillation reconstructions in Figure S4. Figure S5 shows the same reconstruction curves for early stopping. Finally, Figure S6 shows the same curves for multi-class classification.

S7.3. Reconstructions when $N < M$

Figure S7 and Figure S8 show the resulting reconstructions when reconstructing 20 images from a dataset that may contain up to 500 images. Reconstructions are made from 4096 networks with linearized dynamics.

S7.4. Reconstruction Images

Here we show all the reconstruction images and their nearest training images in terms of L_2 distance. Images are sorted based on their rank in the reconstruction curve.

S7.4.1. Binary Classification

We show the reconstruction curves for MNIST Odd vs. Even and CIFAR-10 Animal vs. Vehicle tasks for width 4096 and 1024 networks with linearized or standard dynamics in figures S9 to S16.

S7.4.2. Multiclass Classification

We show the reconstruction curves for MNIST and CIFAR-10 10-way classification for width 4096 and 1024 networks with linearized or standard dyanmics in figures S17 to S24.

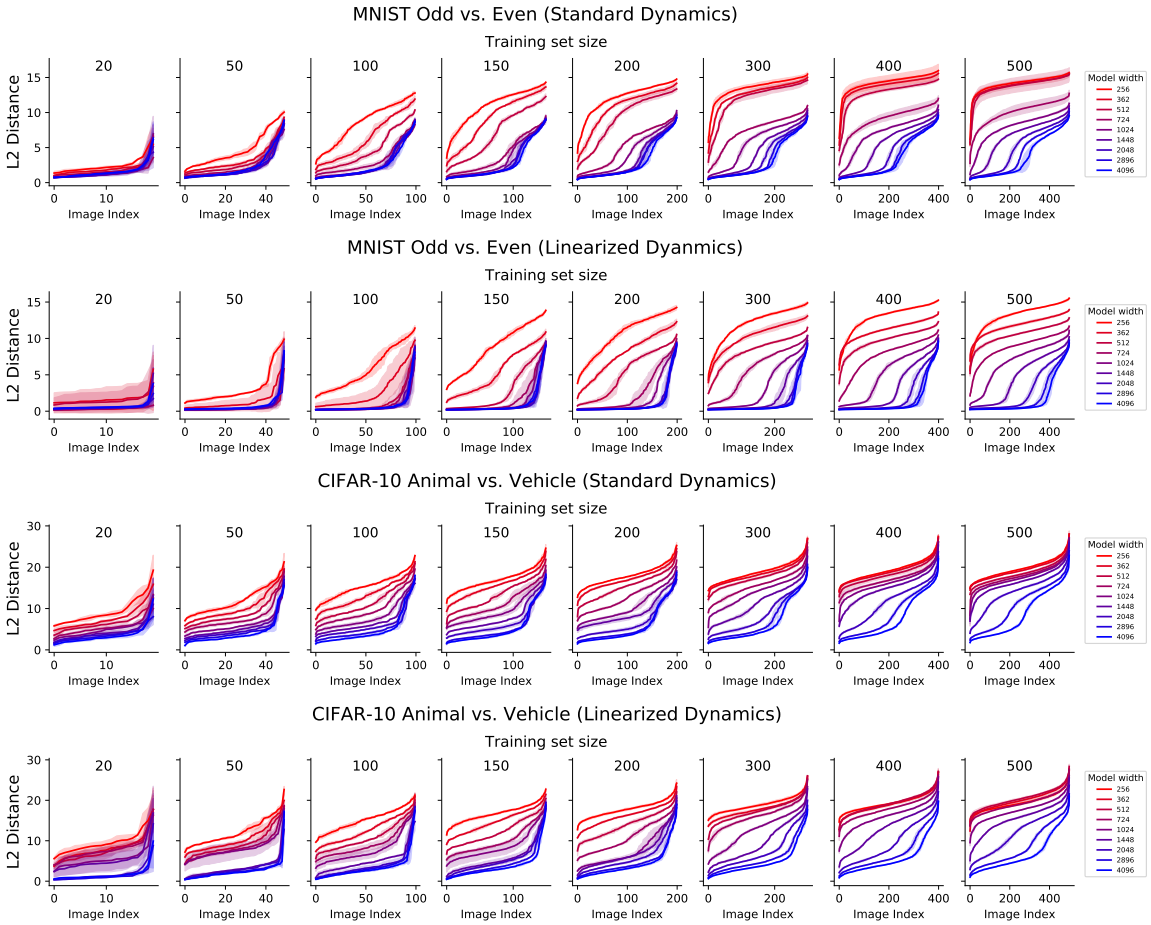

Fig. S3: Reconstruction curves for binary classification tasks

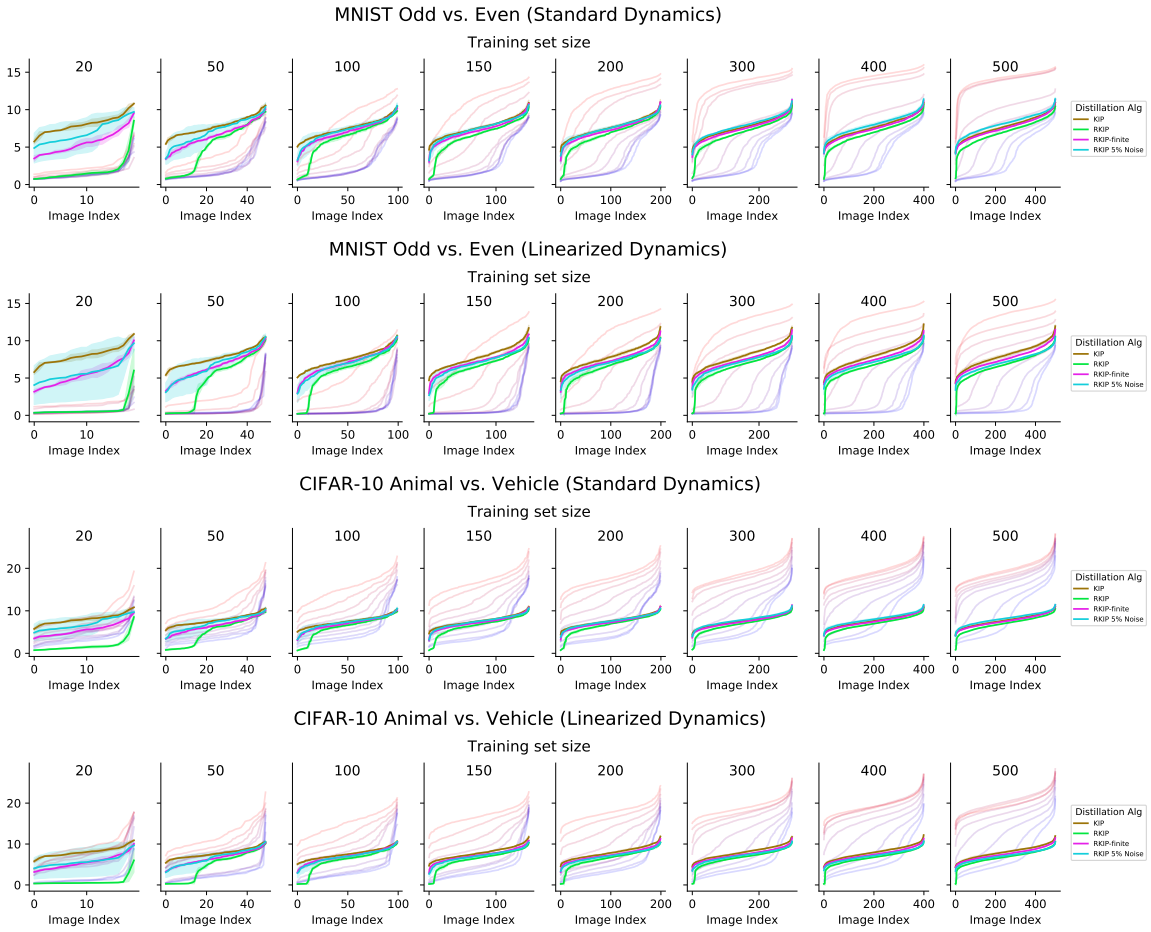

Fig. S4: Reconstruction curves for binary classification tasks with reconstruction curves after training on distilled data

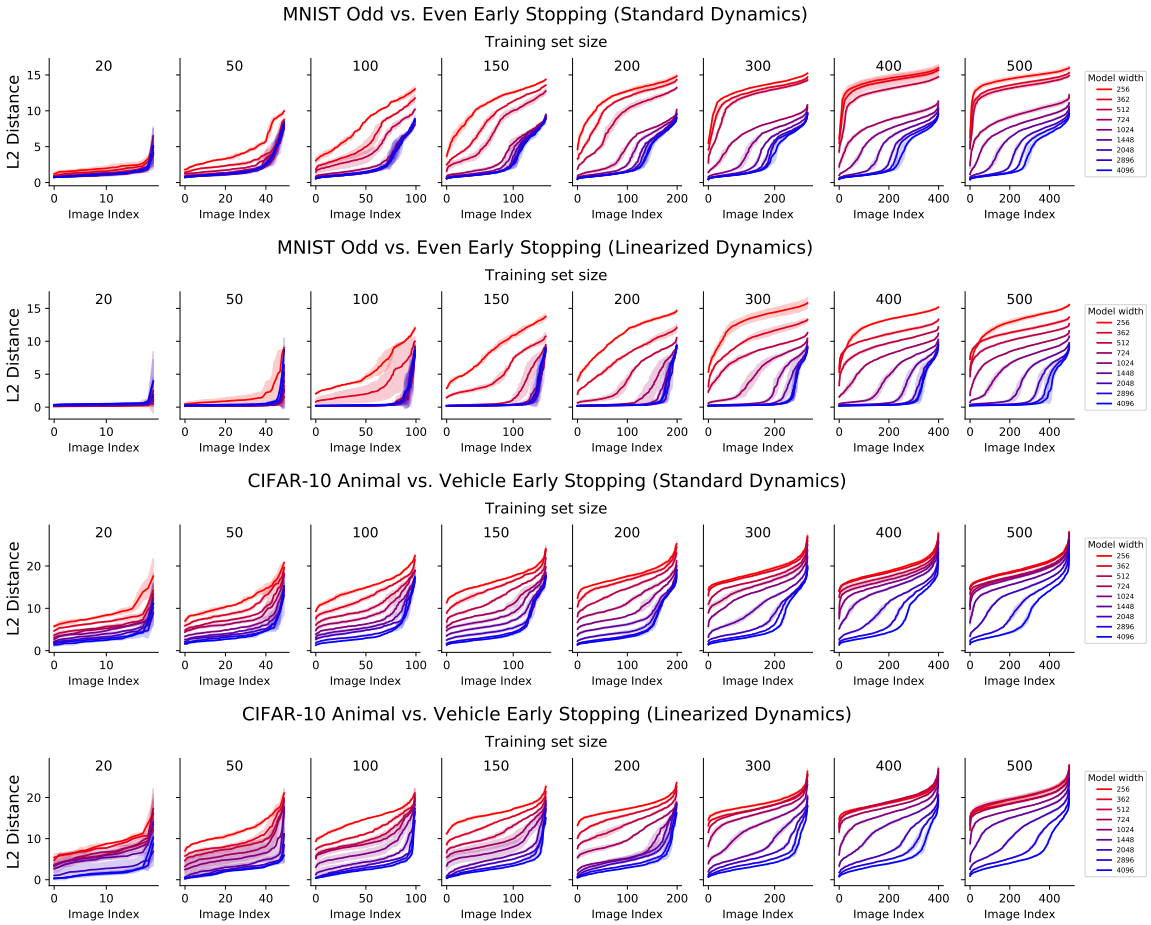

Fig. S5: Reconstruction curves for binary classification tasks with early stopping

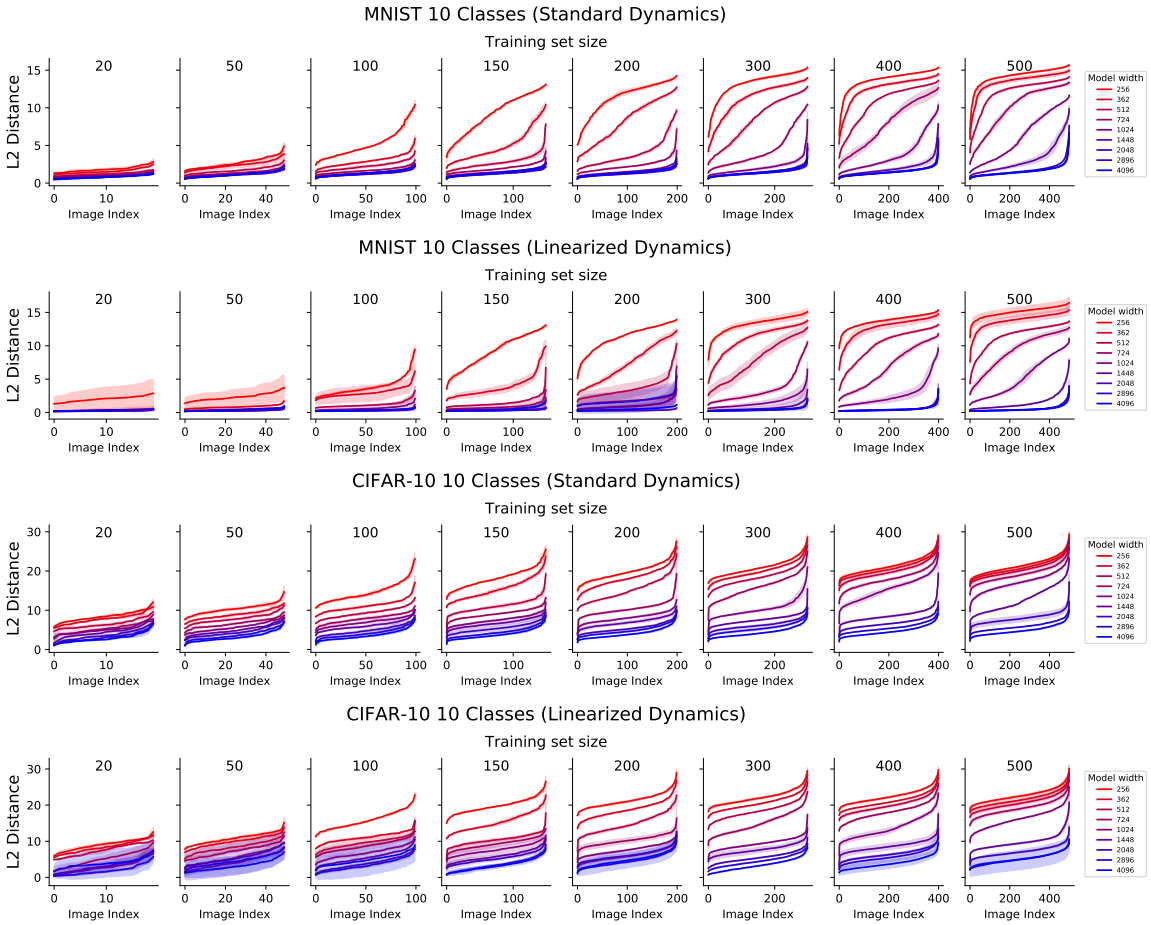

Fig. S6: Reconstruction curves for multiclass classification

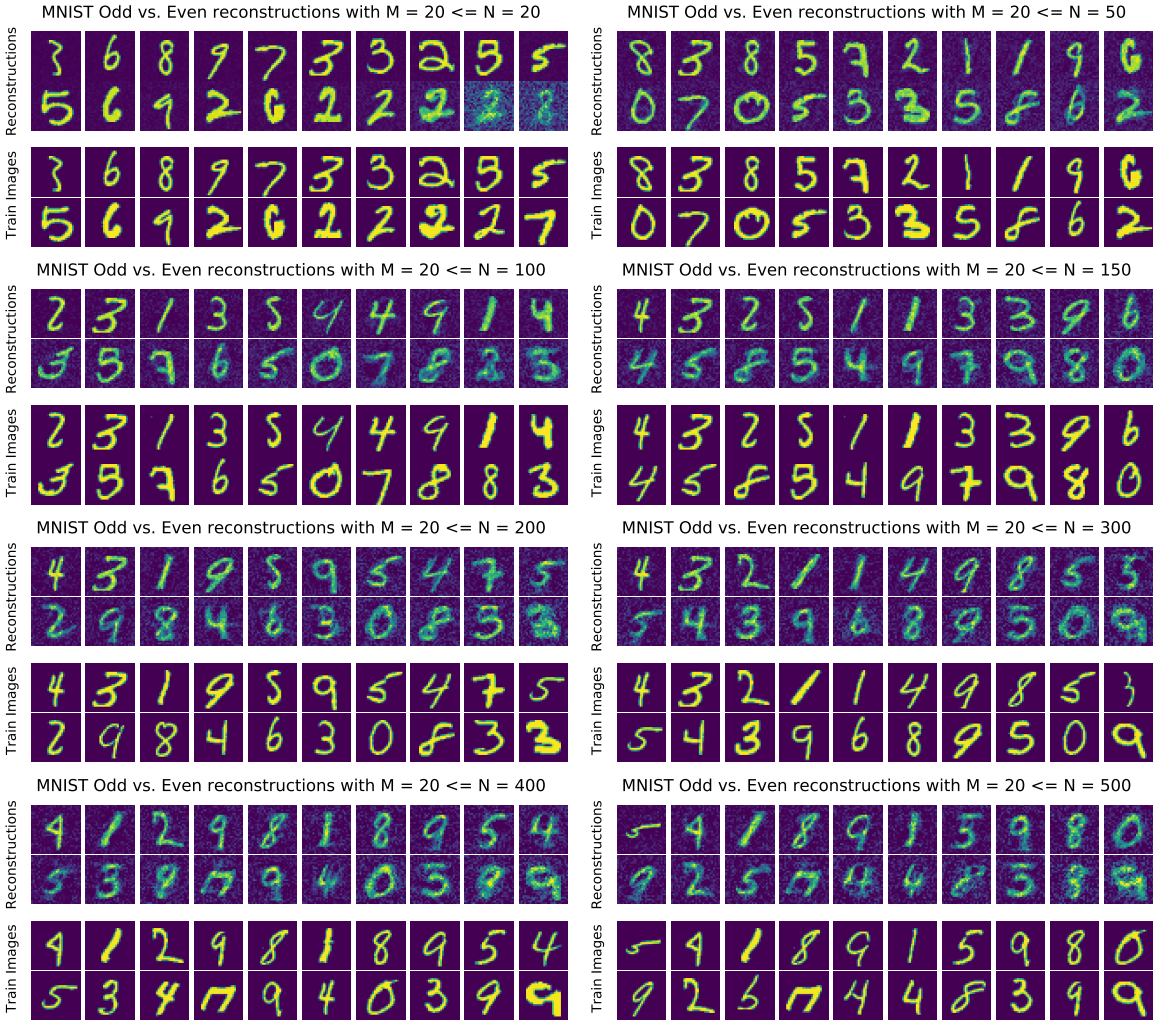

Fig. S7: Reconstructing 20 images from a dataset that may be larger than 20 images (MNIST Odd vs. Even)

Fig. S8: Reconstructing 20 images from a dataset that may be larger than 20 images (CIFAR-10 Animal vs. Vehicle)

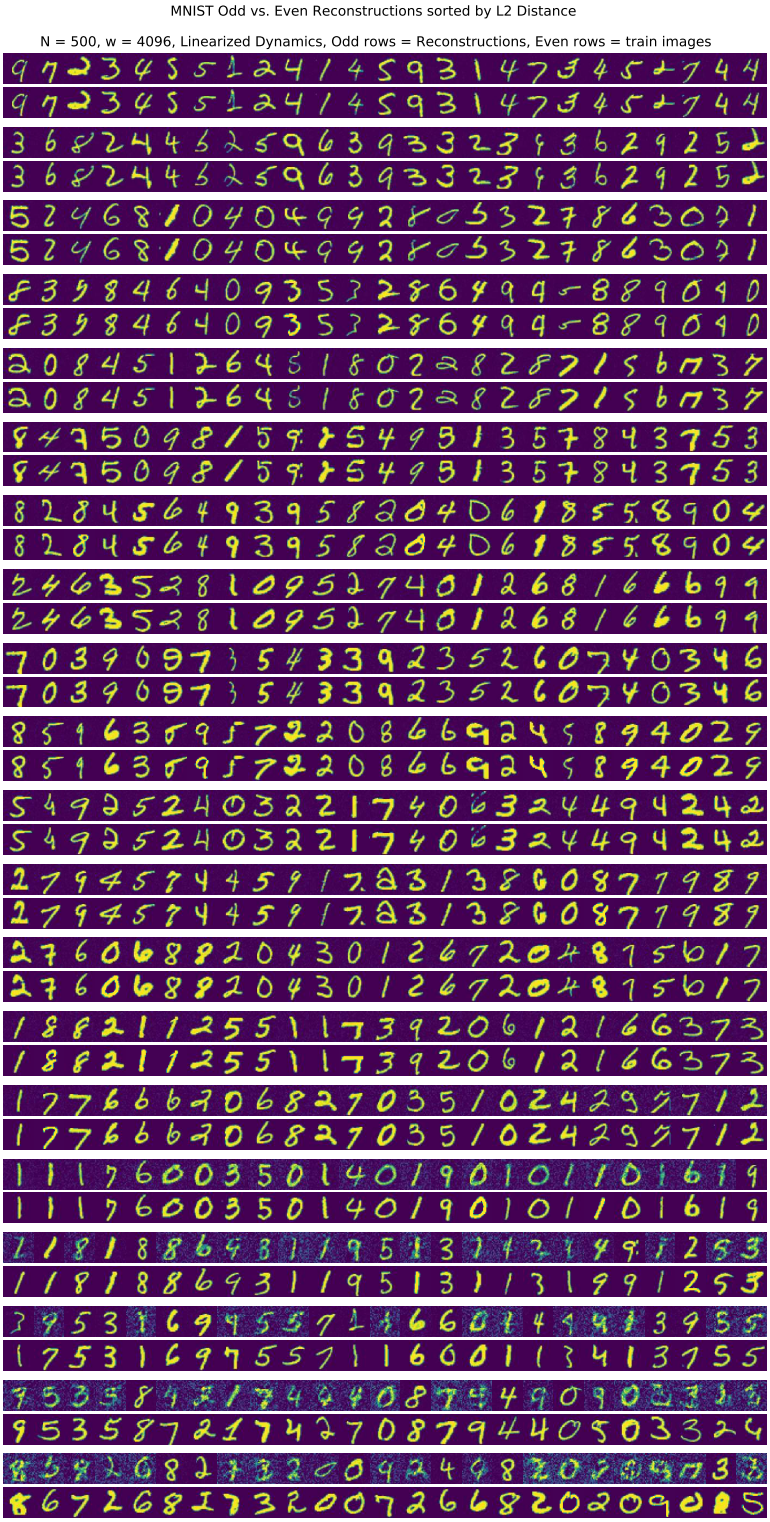

Fig. S9: Reconstructions for MNIST Odd vs. Even, Linearized Dynamics, 4096 width.

Fig. S10: Reconstructions for MNIST Odd vs. Even, Standard Dynamics, 4096 width.

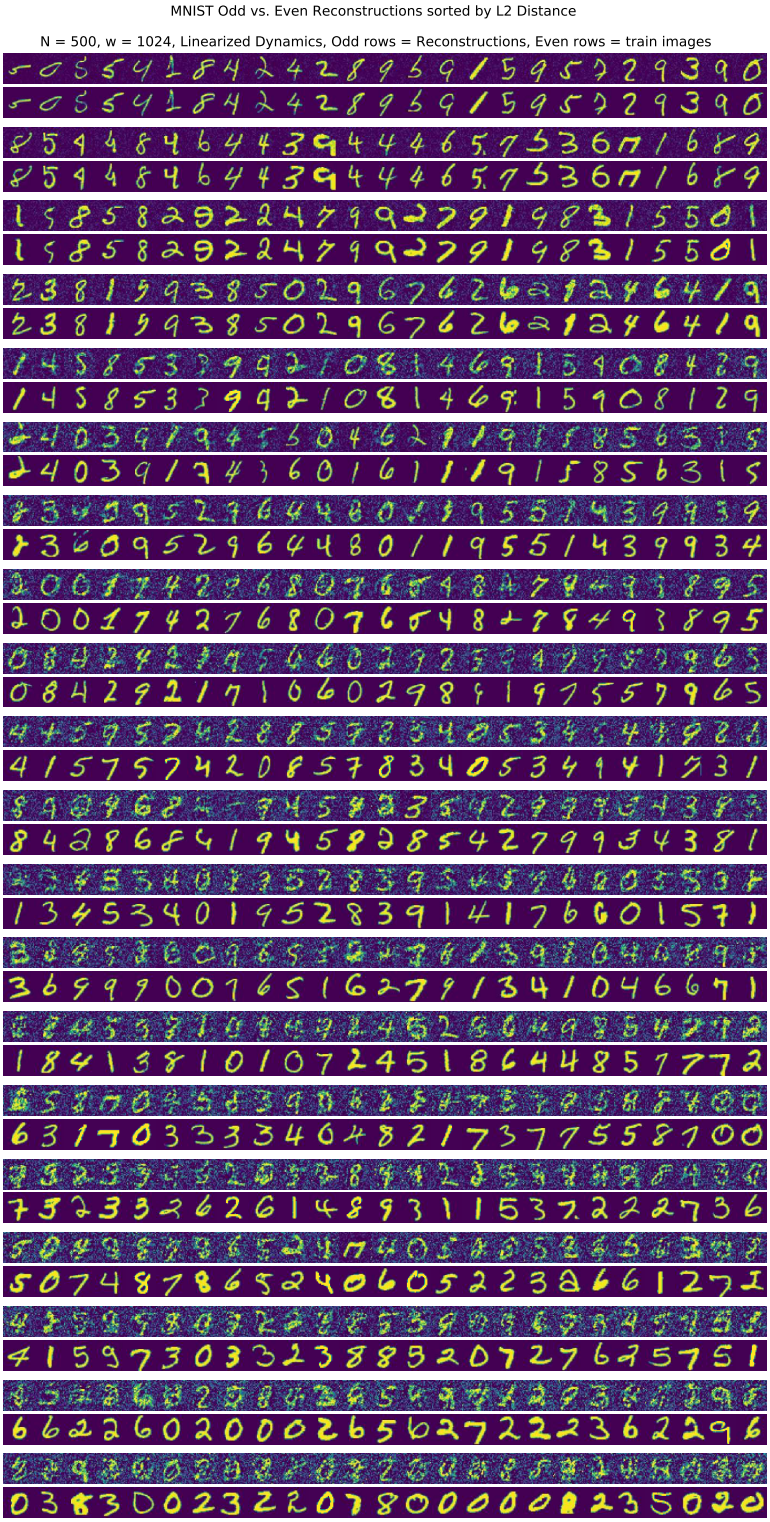

Fig. S11: Reconstructions for MNIST Odd vs. Even, Linearized Dynamics, 1024 width.

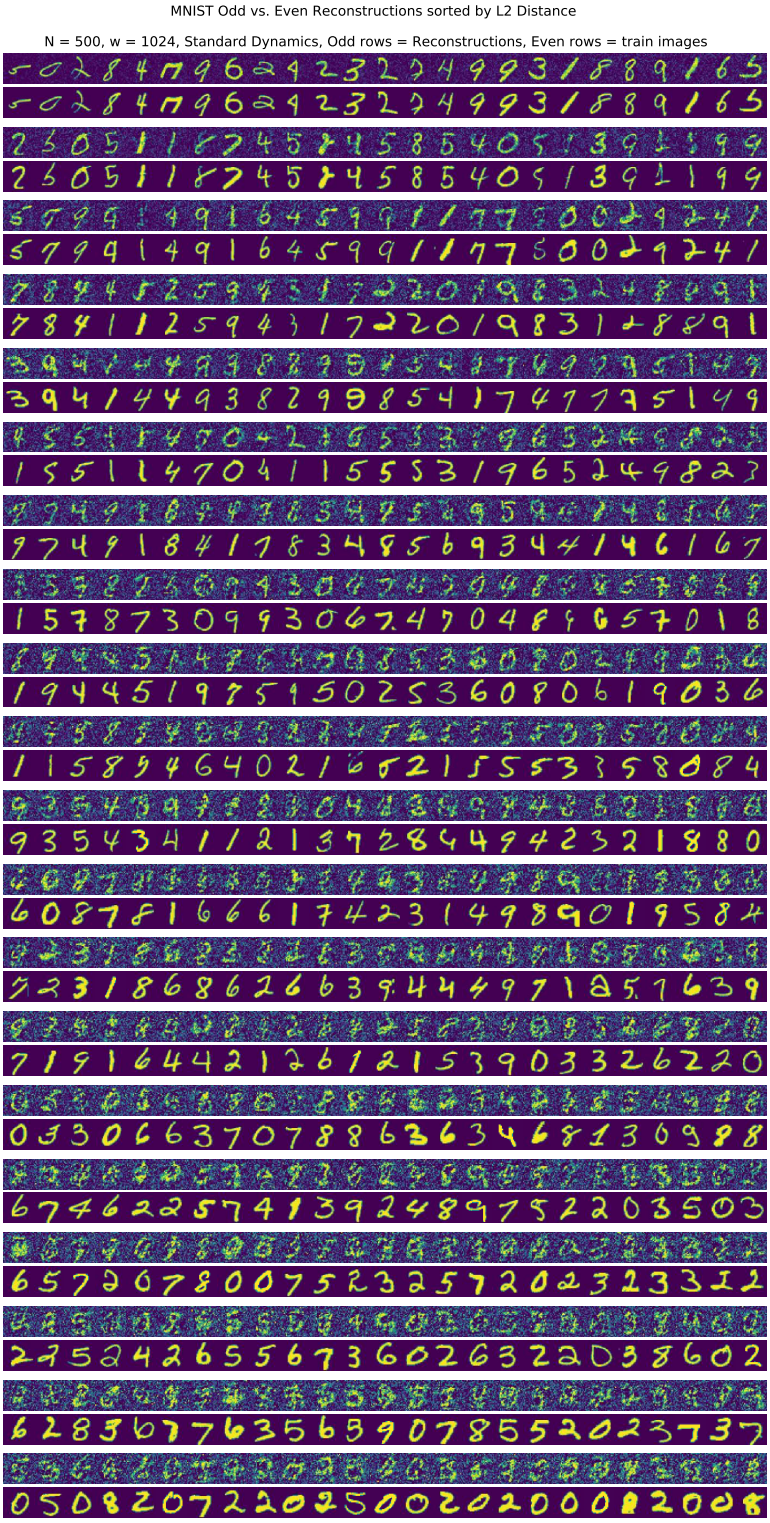

Fig. S12: Reconstructions for MNIST Odd vs. Even, Standard Dynamics, 1024 width.

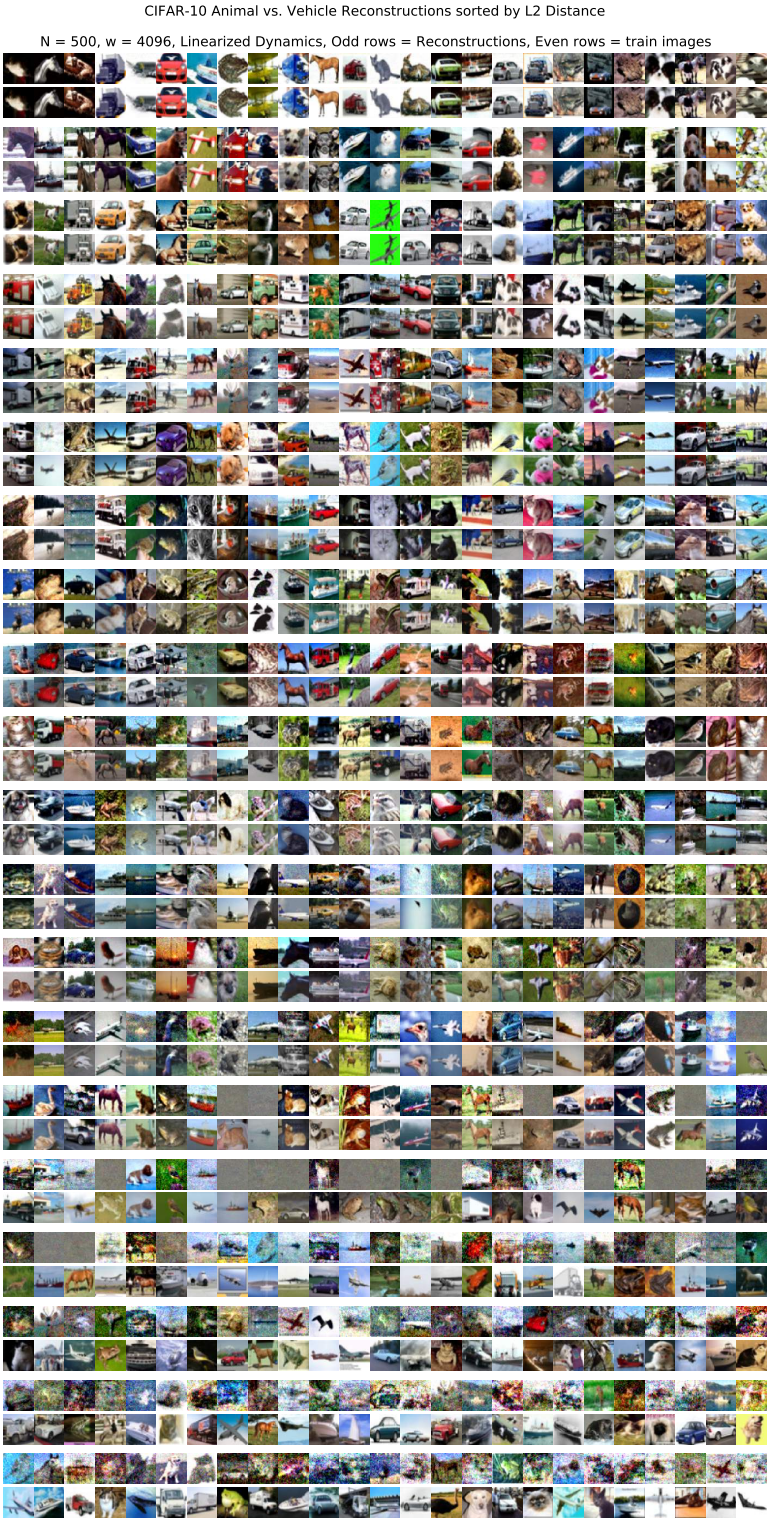

Fig. S13: Reconstructions for CIFAR-10 Animal vs. Vehicle, Linearized Dynamics, 4096 width.

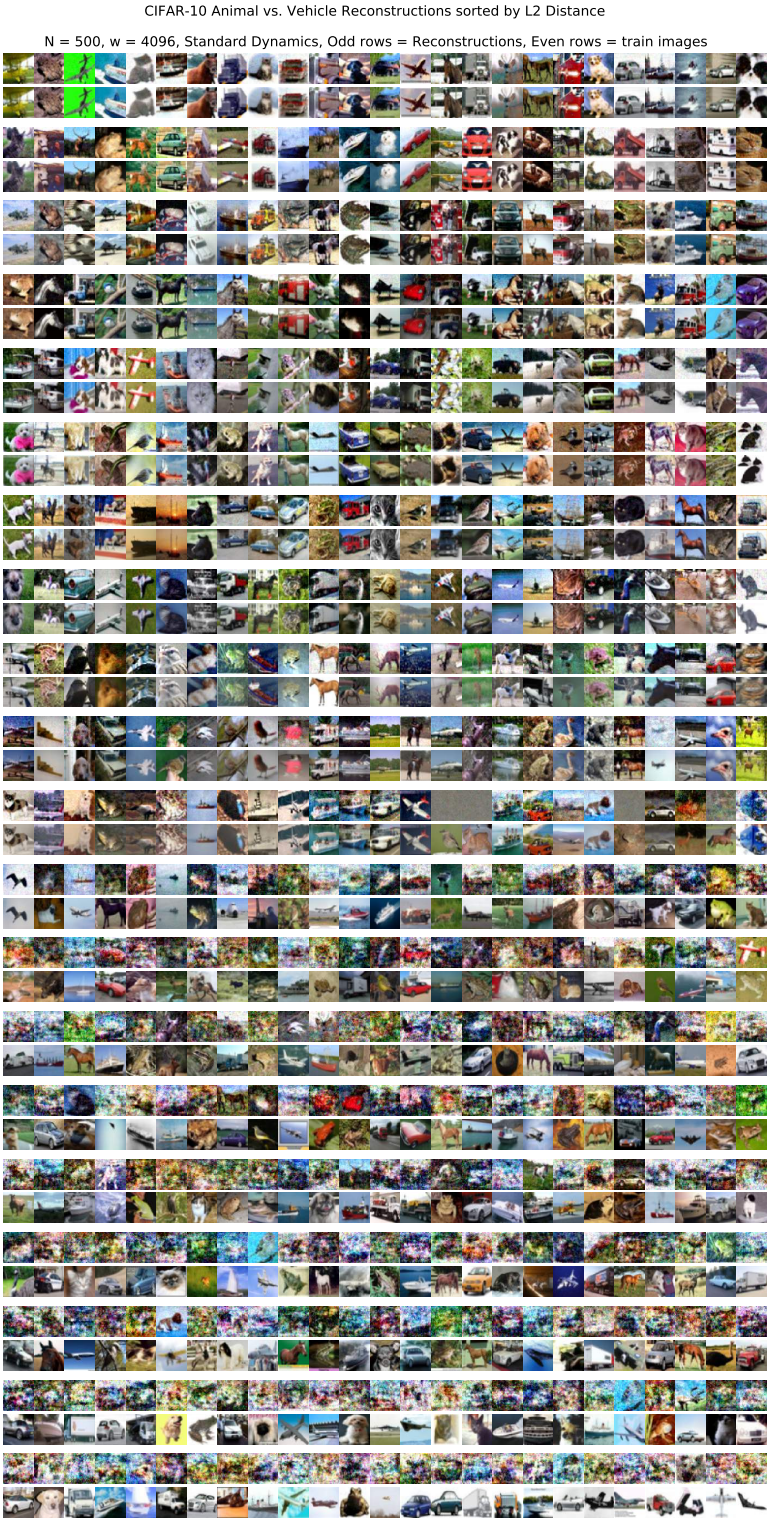

Fig. S14: Reconstructions for CIFAR-10 Animal vs. Vehicle, Standard Dynamics, 4096 width.

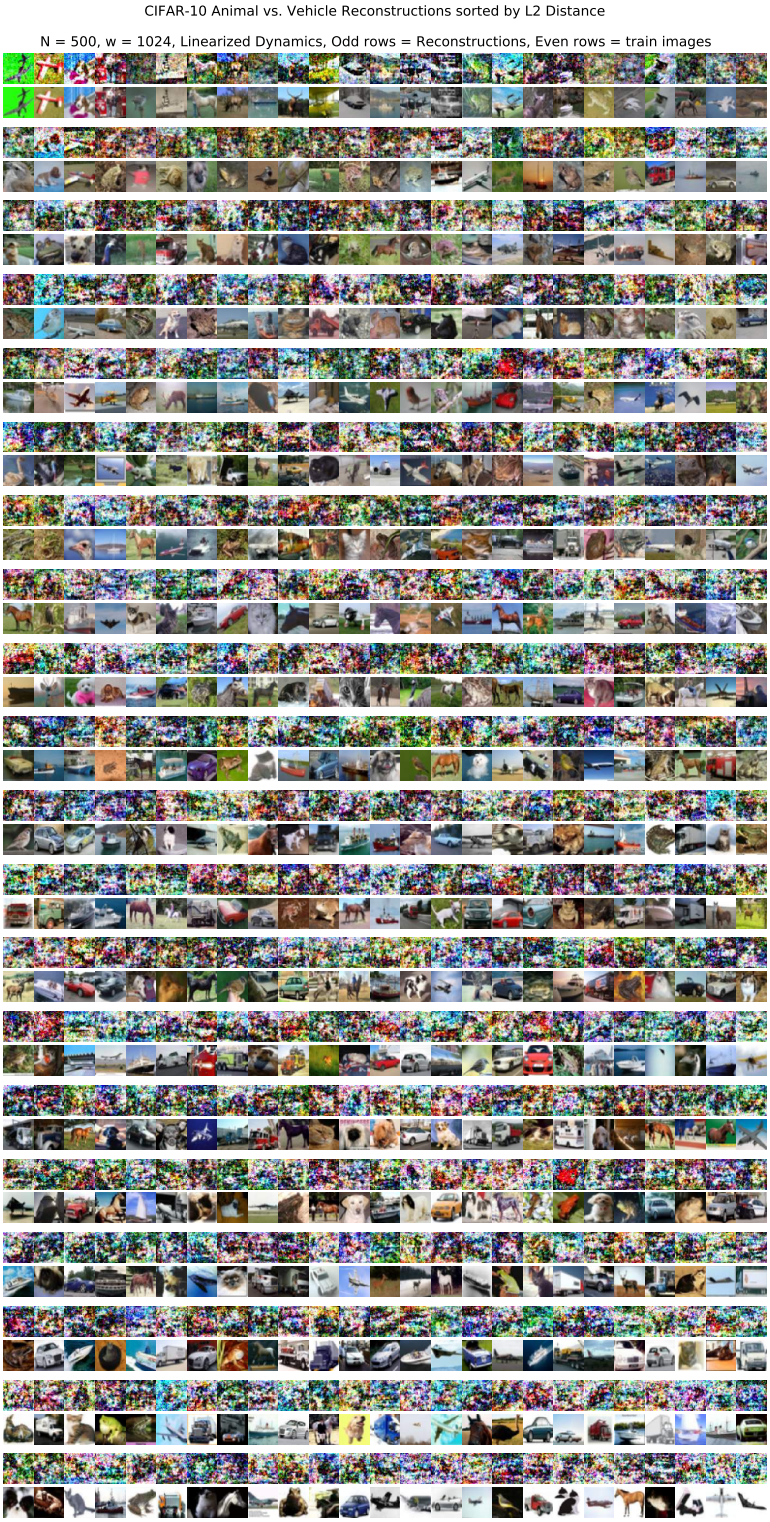

Fig. S15: Reconstructions for CIFAR-10 Animal vs. Vehicle, Linearized Dynamics, 1024 width.

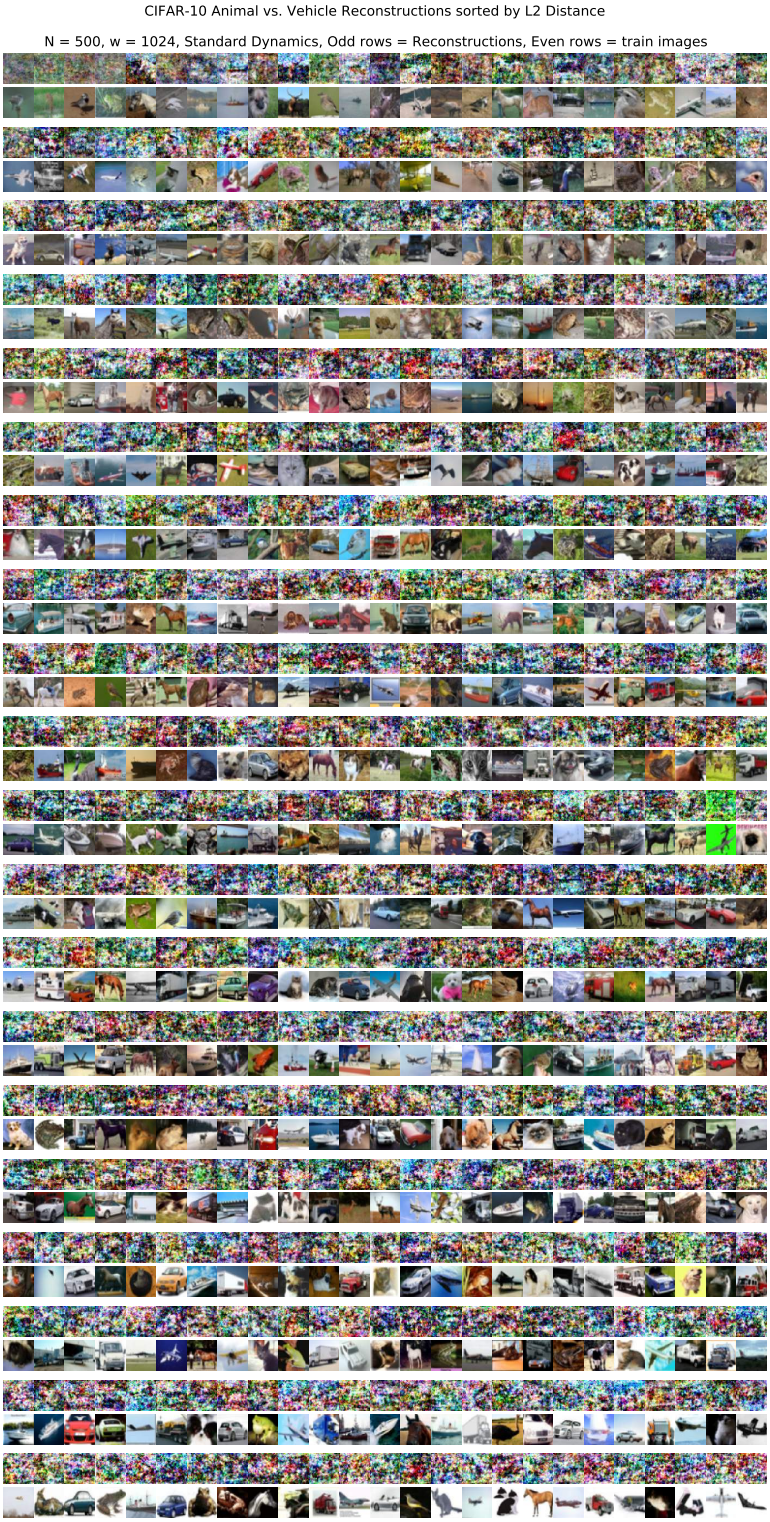

Fig. S16: Reconstructions for CIFAR-10 Animal vs. Vehicle, Standard Dynamics, 1024 width.

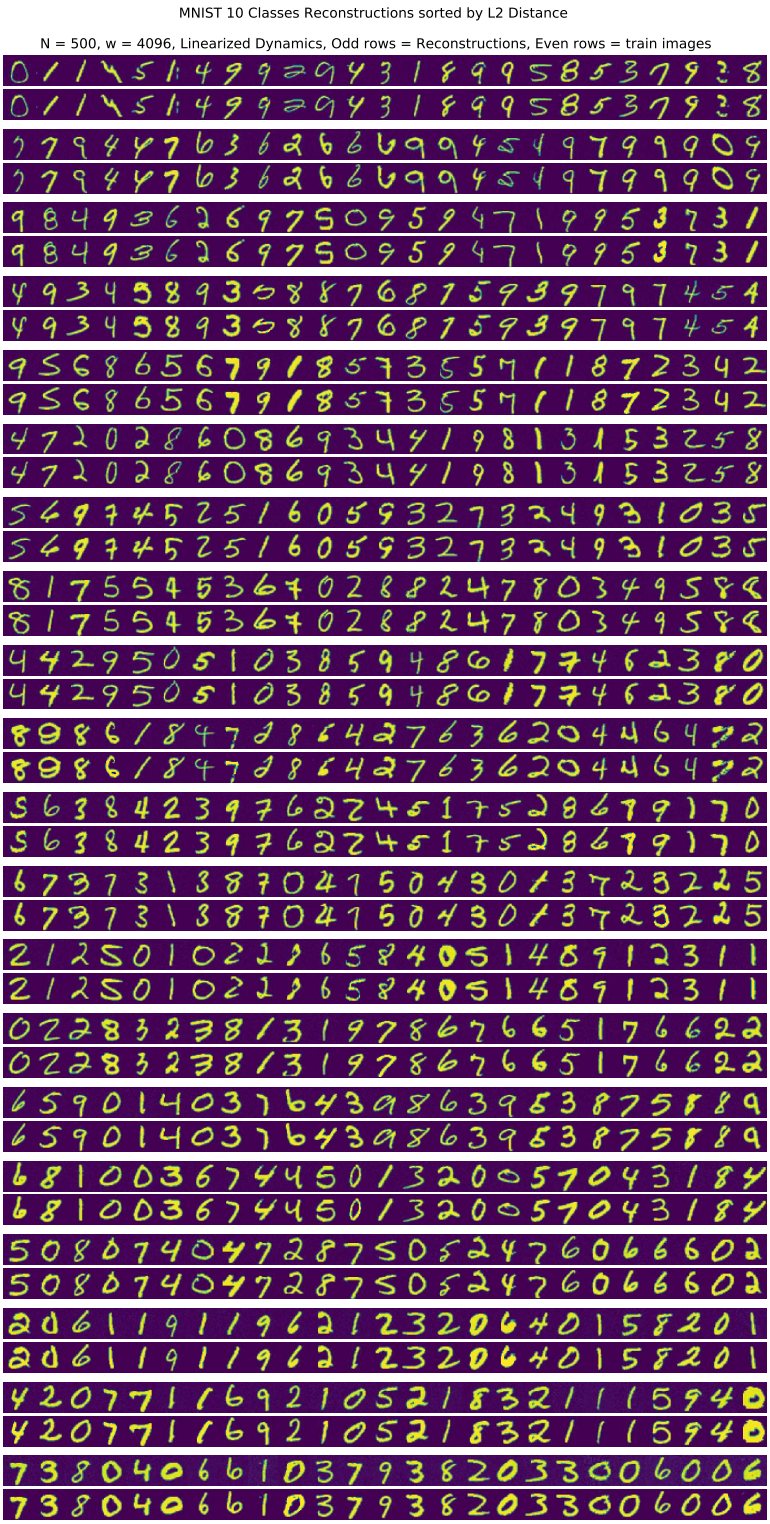

Fig. S17: Reconstructions for MNIST 10 Classes, Linearized Dynamics, 4096 width.

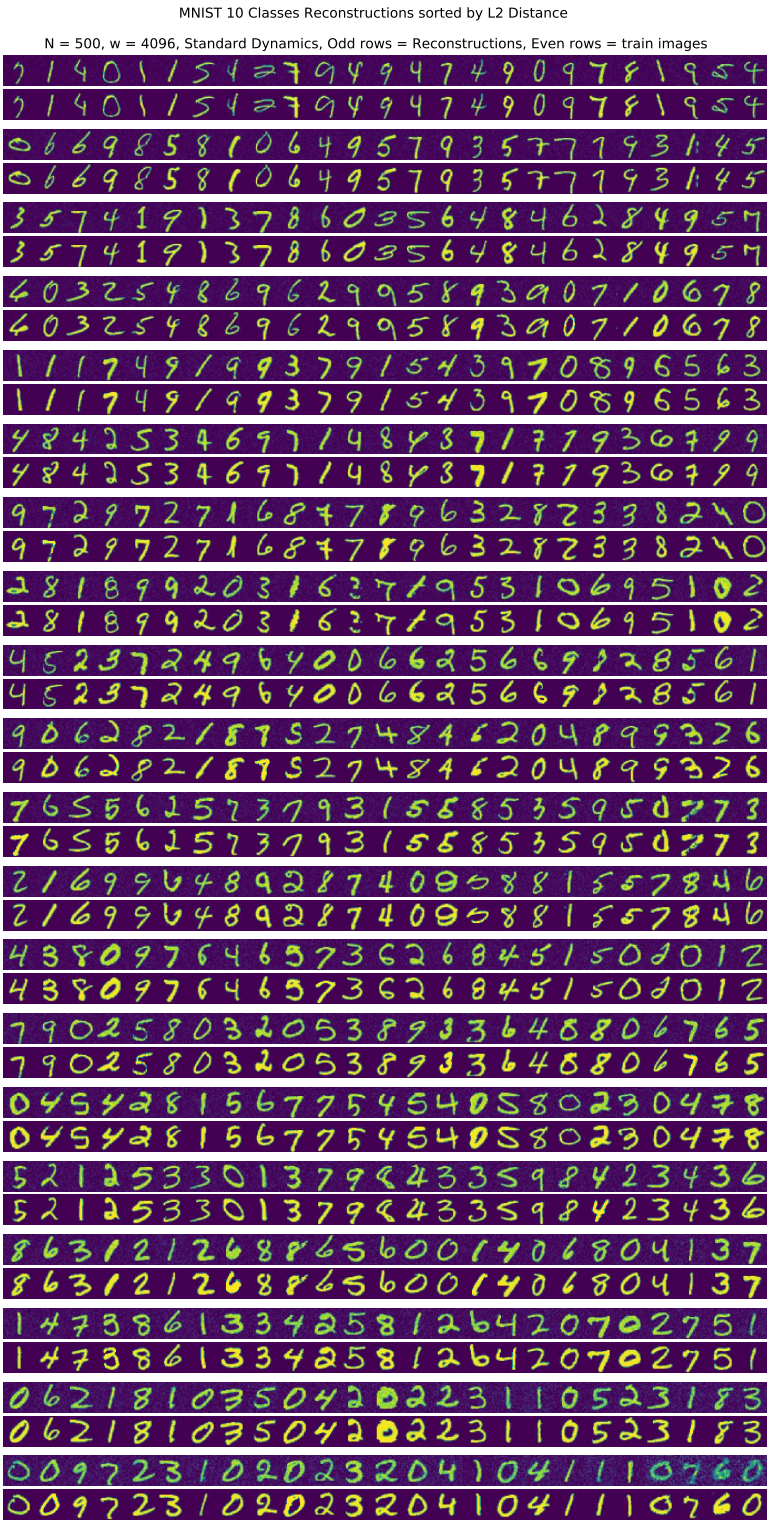

Fig. S18: Reconstructions for MNIST 10 Classes, Standard Dynamics, 4096 width.

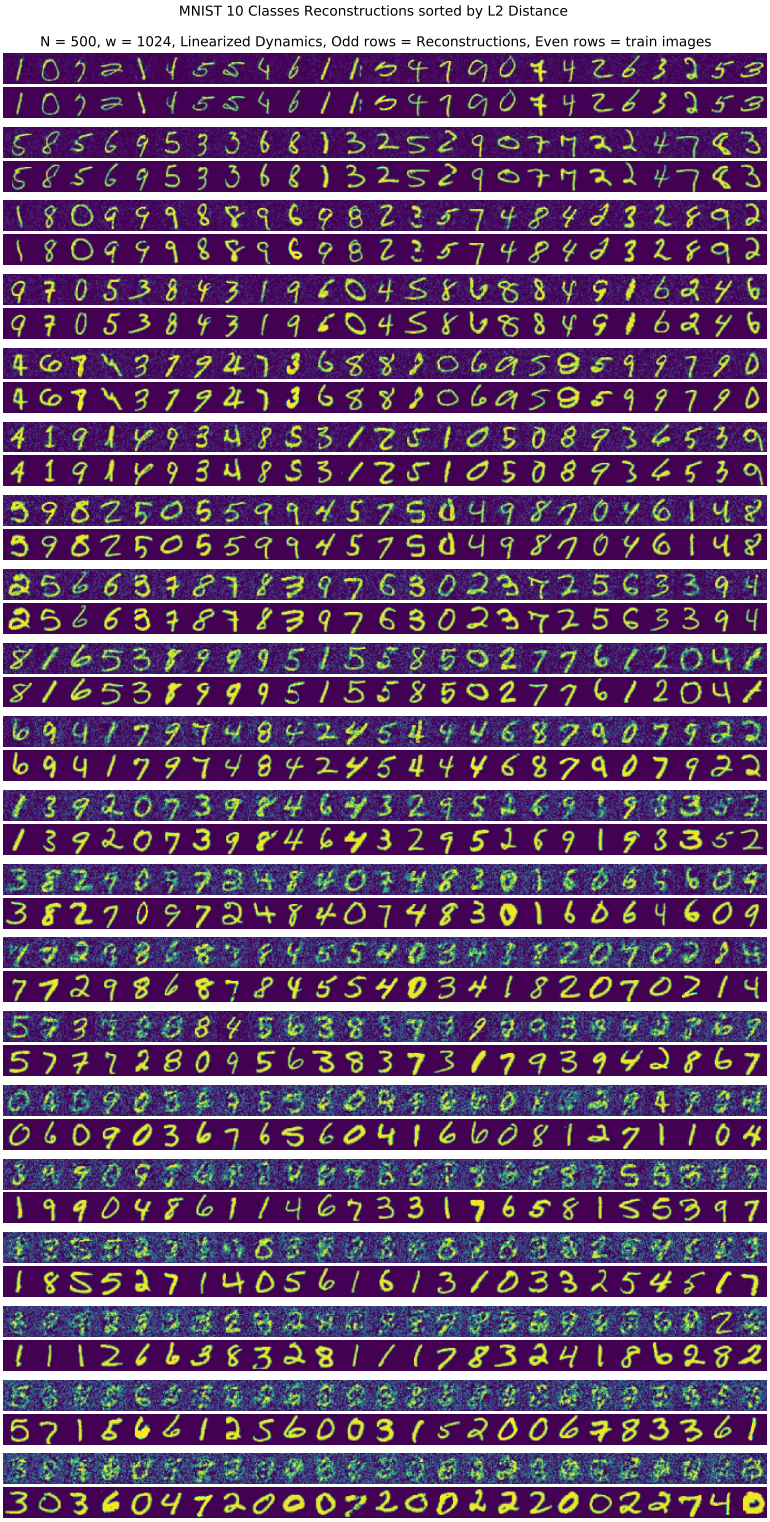

Fig. S19: Reconstructions for MNIST 10 Classes, Linearized Dynamics, 1024 width.

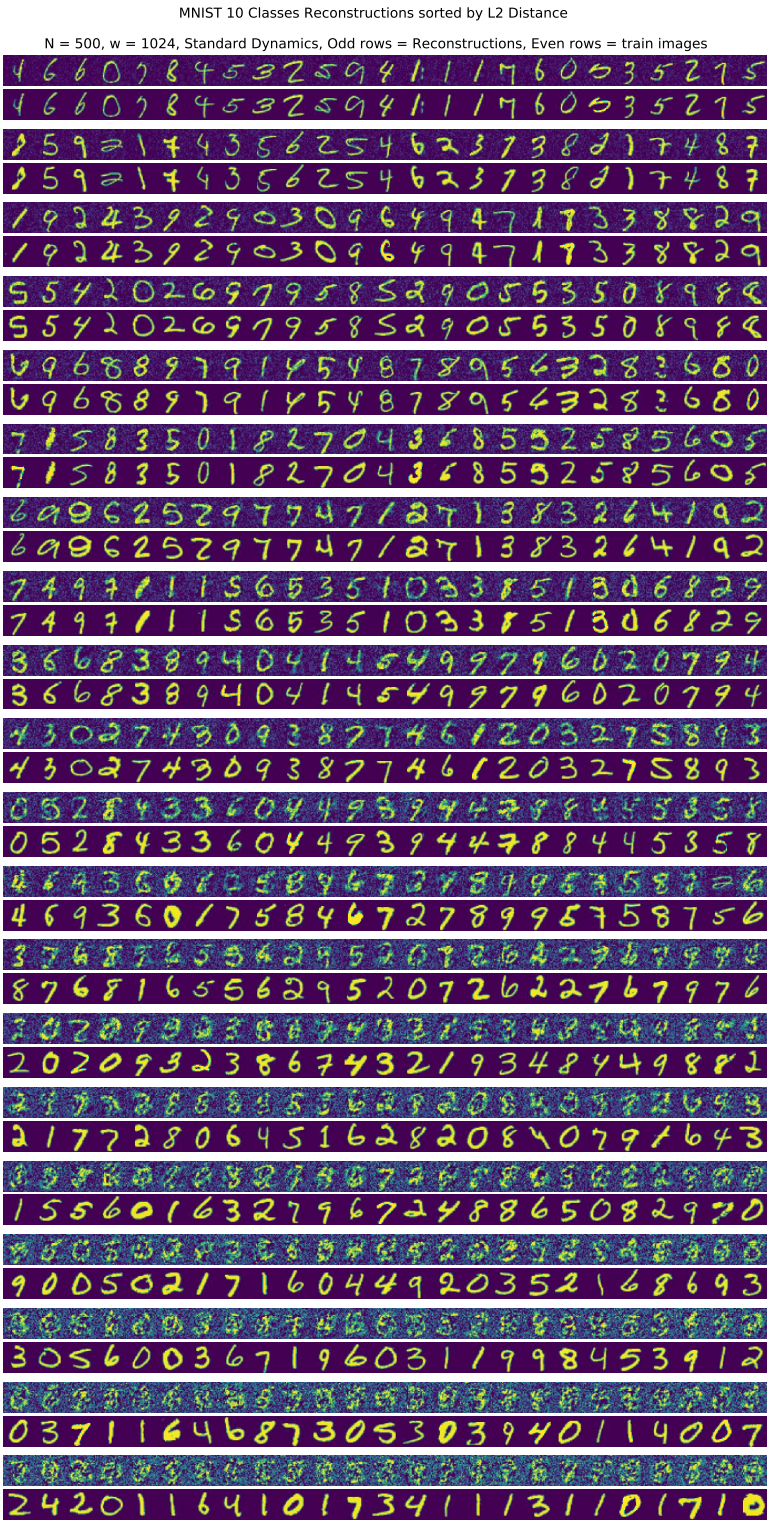

Fig. S20: Reconstructions for MNIST 10 Classes, Standard Dynamics, 1024 width.

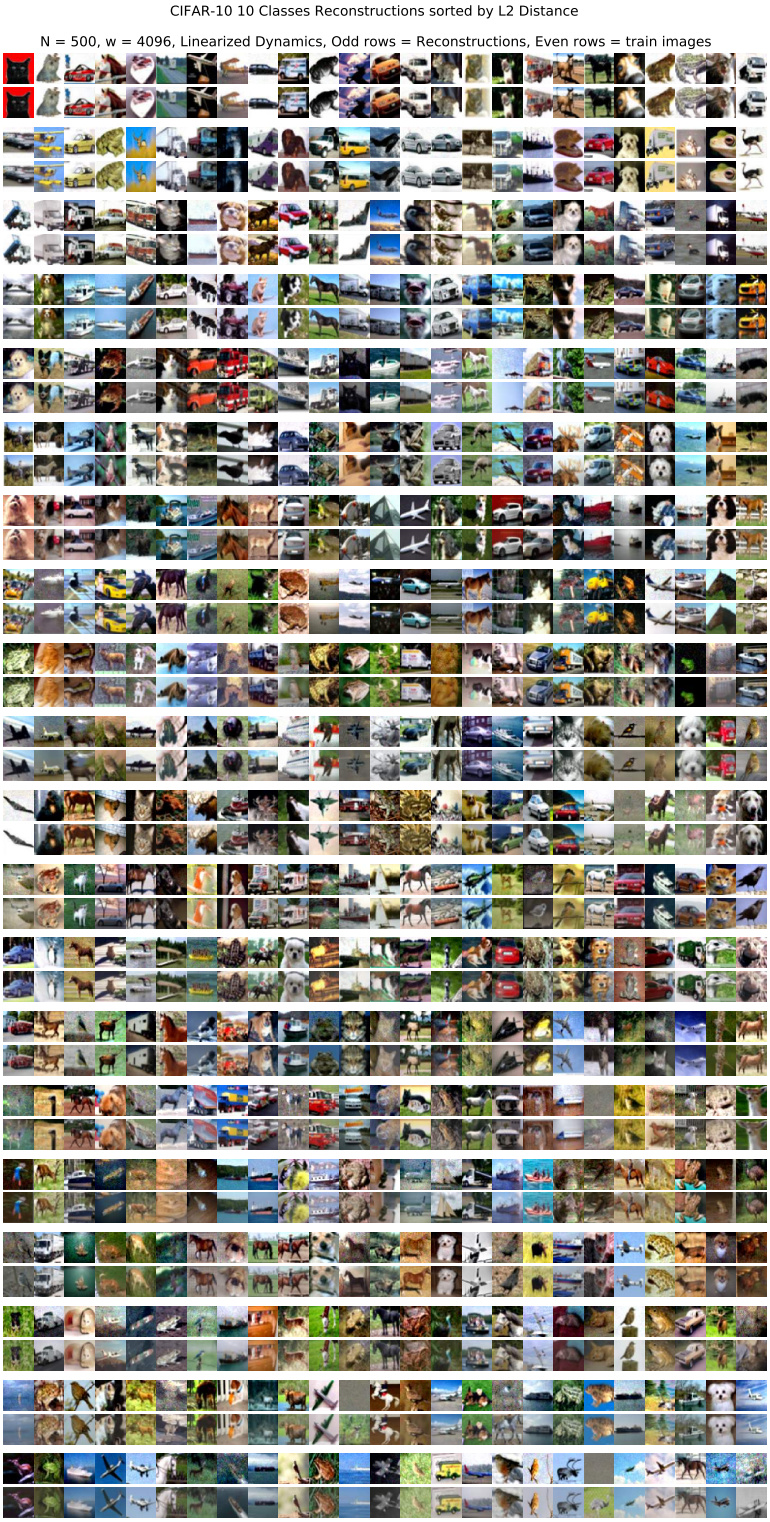

Fig. S21: Reconstructions for CIFAR-10 10 Classes, Linearized Dynamics, 4096 width.

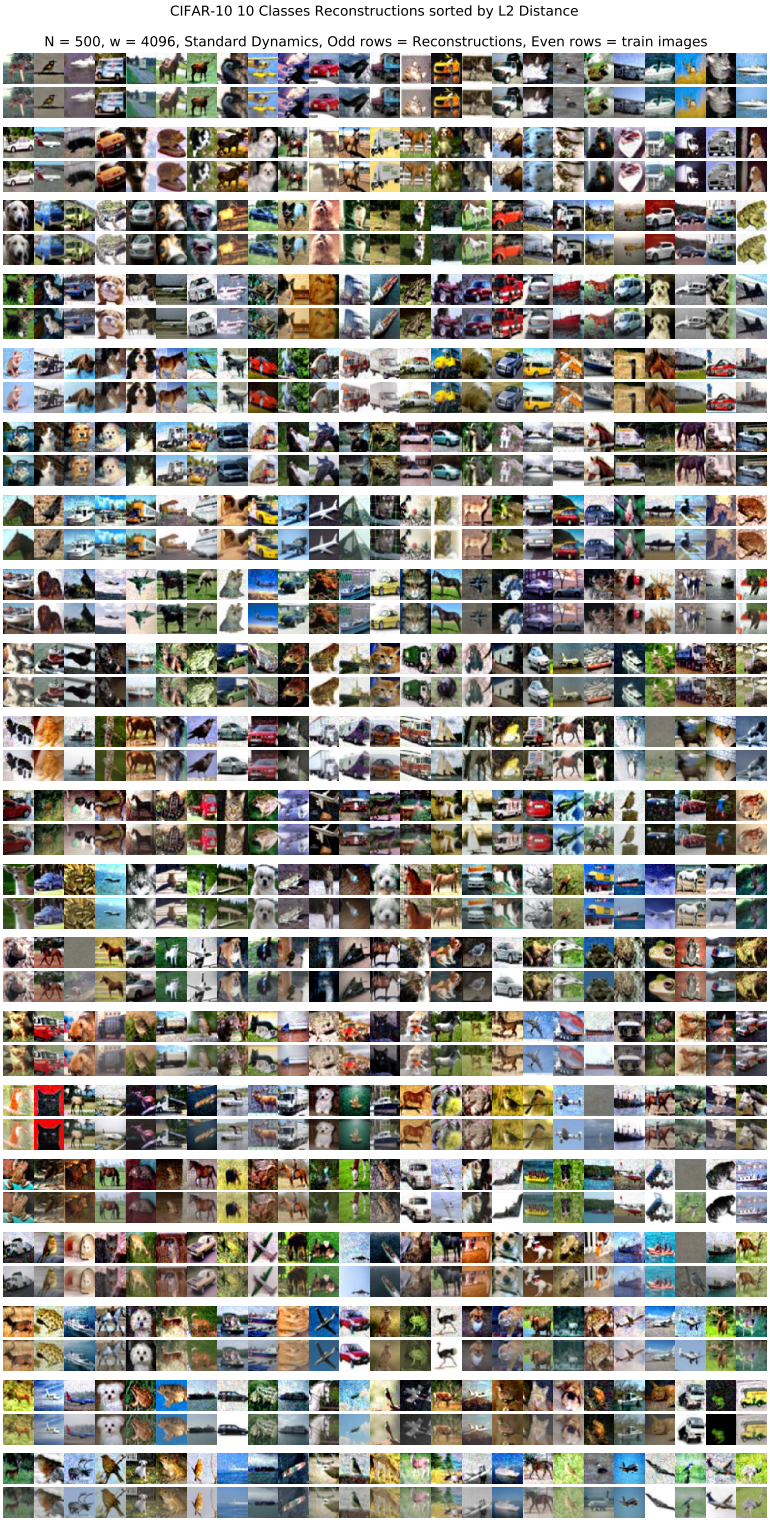

Fig. S22: Reconstructions for CIFAR-10 10 Classes, Standard Dynamics, 4096 width.

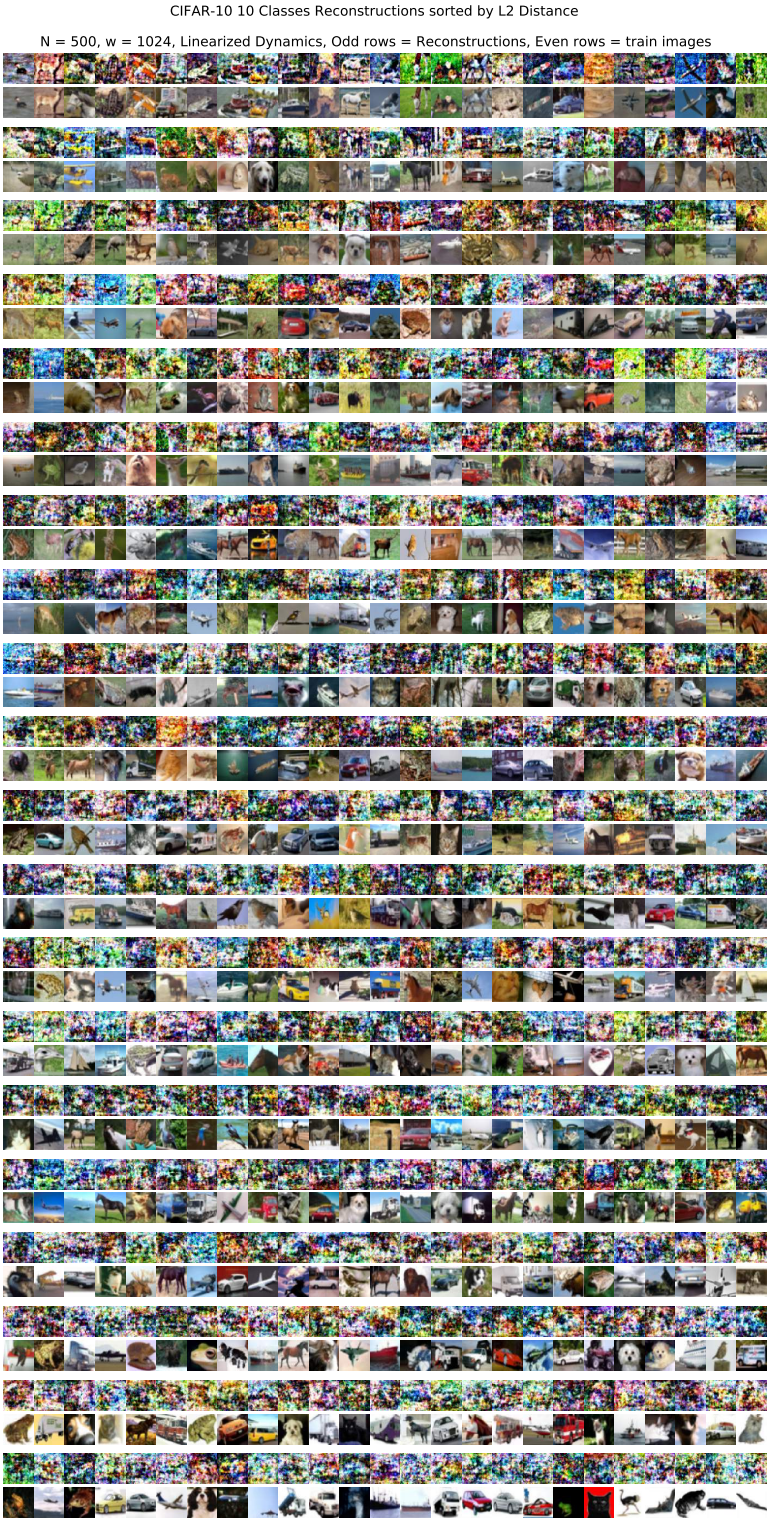

Fig. S23: Reconstructions for CIFAR-10 A10 Classes, Linearized Dynamics, 1024 width.

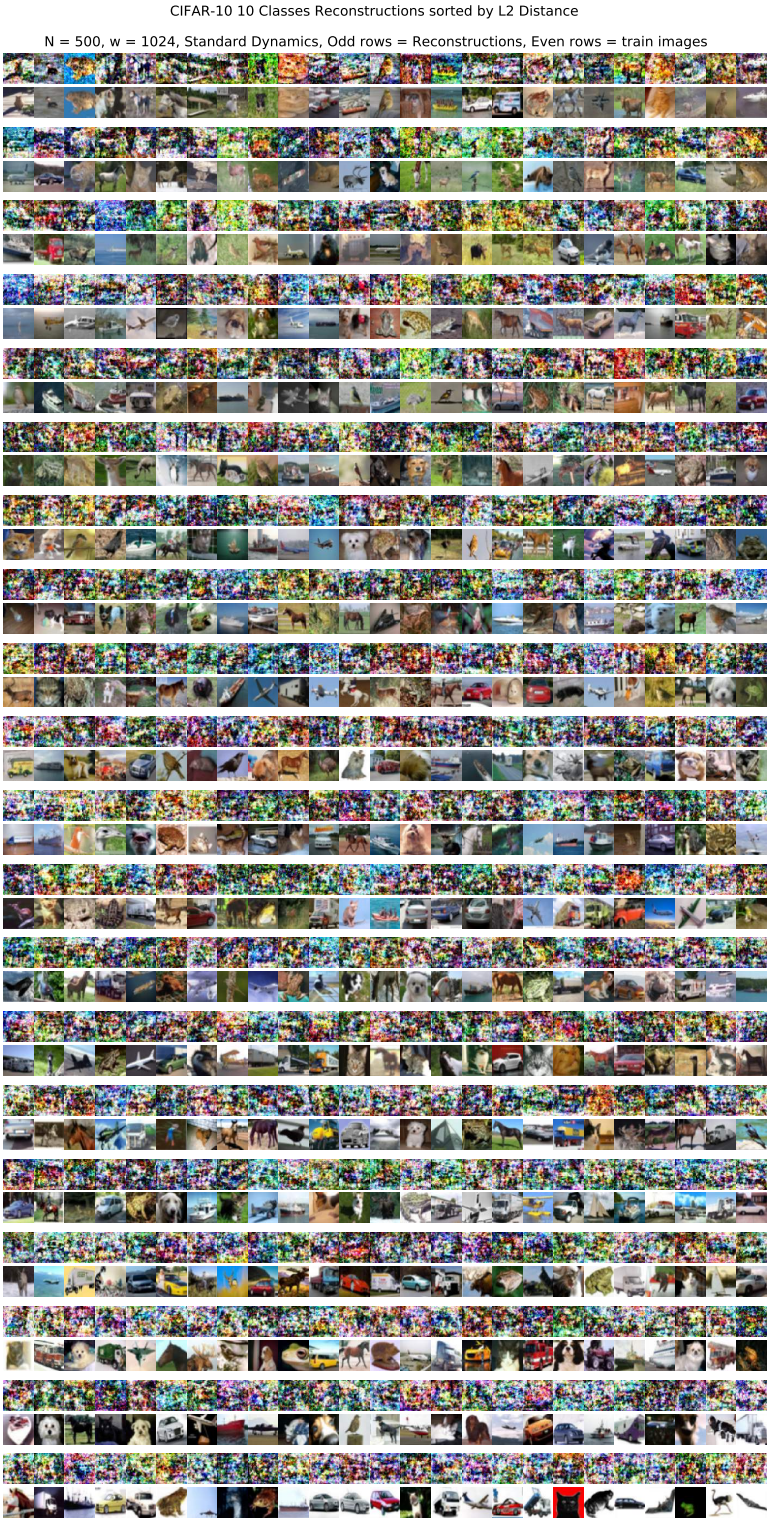

Fig. S24: Reconstructions for CIFAR-10 10 Classes, Standard Dynamics, 1024 width.